Published in final edited form as:

Mol Cell. 2021 September 02; 81(17): 3496–3508.e5. doi:10.1016/j.molcel.2021.07.023.

Structure of an Hsp90-immunophilin complex reveals cochaperone recognition of the client-maturation state

Kanghyun Lee[1], **Aye C. Thwin**[1], **Cory M. Nadel**[1], **Eric Tse**[1], **Stephanie N. Gates**[2], **Jason E. Gestwicki**[1,3], **Daniel R. Southworth**[1,4,*]

[1]Institute for Neurodegenerative Diseases, University of California, San Francisco, CA 94158, USA

[2]Graduate Program in Chemical Biology, University of Michigan, Ann Arbor, MI, USA. Current address: Department of Molecular and Cell Biology, University of California, Berkeley, CA 94720, USA

[3]Department of Pharmaceutical Chemistry, University of California, San Francisco, CA 94158, USA

[4]Department of Biochemistry and Biophysics, University of California, San Francisco, CA 94158, USA

Summary

The Hsp90 chaperone promotes the folding and activation of hundreds of client proteins in the cell through an ATP-dependent conformational cycle guided by distinct cochaperone regulators. The FKBP51 immunophilin binds Hsp90 with its tetratricopeptide repeat (TPR) domain and catalyzes peptidyl-prolyl isomerase (PPIase) activity during the folding of kinases, nuclear receptors and tau. Here we have determined the cryo-EM structure of the human Hsp90:FKBP51:p23 complex to 3.3 Å that, together with mutagenesis and crosslinking analysis, reveals the basis for cochaperone binding to Hsp90 during client maturation. A helix extension in the TPR functions as a key recognition element, interacting across the Hsp90 C-terminal dimer interface presented in the closed, ATP conformation. The PPIase domain is positioned along the middle domain, adjacent Hsp90 client binding sites, while a single p23 makes stabilizing interactions with the N-terminal dimer. With this architecture, FKBP51 is positioned to act on specific client residues presented during Hsp90-catalyzed remodeling.

Graphical Abstract

[*]Lead Contact, Correspondence to: D.R.S. (daniel.southworth@ucsf.edu).

Author Contributions

K.L. performed biochemical and cryo-EM experiments, developed figures and wrote and edited the manuscript. A.C.T. generated mutant constructs and expressed and purified proteins. C.M.N. performed FP data analysis. E.T. operated the Krios microscope and helped with data collection and structure determination. S.N.G. performed initial biochemical and cryo-EM analysis and edited the manuscript. J.E.G advised and edited the manuscript. D.R.S. designed and supervised the project and wrote and edited the manuscript.

Declaration of Interests

The authors declare no competing interests.

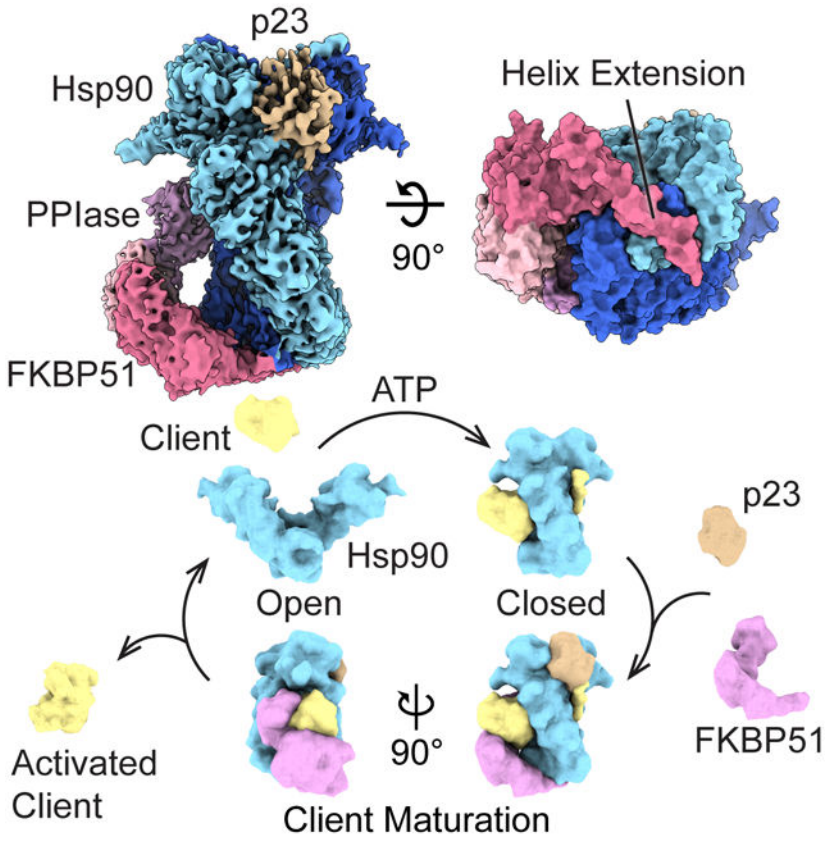

In Brief

Hsp90-cochaperone complexes coordinate to promote activation of hundreds of client proteins. Lee et al. determine cryo-EM structures of the Hsp90:FKBP51:p23 complex, revealing a closed ATP state for client maturation and recognition mechanism of the FKBP51 prolyl isomerase. With this architecture, FKBP51 may act on specific client sites presented by Hsp90.

Introduction

Heat shock protein (Hsp) 90 is a universally conserved molecular chaperone that is critical to the human proteome through the folding and activation of numerous client protein substrates such as nuclear hormone receptors (glucocorticoid and estrogen receptors), transcription factors (HSF1, p53, and OCT4) and kinases (BRAF, Cdk4, and ErbB2/Her2) (Schopf et al., 2017). Hsp90 is upregulated in cancer cells (Whitesell and Lindquist, 2005) and many oncoproteins, such as Bcr-Abl (An et al., 2000) and ErbB2/Her2 (Xu et al., 2001), require Hsp90 interaction. Thus, Hsp90-specific inhibitors, including geldanamycin and its derivatives, are of significant importance as anti-cancer therapeutics (Trepel et al., 2010). Additionally, Hsp90 plays key roles in neurodegenerative disease pathways including regulating Tau modification and folding (Shelton et al., 2017) and inhibiting α-synuclein aggregation (Daturpalli et al., 2013).

Hsp90 forms dynamic macromolecular assemblies with distinct cochaperone proteins that regulate its ATPase cycle and client folding steps (Pearl and Prodromou, 2006). Moreover, the interaction by the tetratricopeptide repeat (TPR) class of cochaperones is critical in conferring distinct Hsp90 folding steps and pathways, such as client loading (Hop), ubiquitination (Chip), and de-phosphorylation (PP5) (Biebl and Buchner, 2019; Smith, 2004). These cochaperones bind the EEVD C-terminal peptide of eukaryotic Hsp90s and Hsp70s via the 7-member α-helical TPR domain, which forms a conserved carboxylate "clamp" interaction with the terminal Asp (Scheufler et al., 2000). However, little is known about the structural basis for their interaction beyond TPR-EEVD binding or how distinct regulatory functions are specified on Hsp90.

The FK506-binding protein 51 (FKBP51), a member of the immunophilin family that includes FKBP52 and Cyp40 TPR-cochaperones, binds Hsp90 but not Hsp70 and catalyzes peptidyl prolyl isomerization (PPI) of clients, regulating their folding and downstream function (Zgajnar et al., 2019). PPIase activity occurs through the N-terminal FK1 domain and is inhibited by immunosuppressive compounds including FK506 and rapamycin (Hahle et al., 2019). FK1 is connected to a related but inactive FK2 domain followed by the C-terminal TPR domain, which together adopt an extended tripartite configuration in the crystal structure (Sinars et al., 2003). Both FKBP51 and the close homolog, FKBP52, are identified in Hsp90:p23 maturation complexes containing the glucocorticoid or other nuclear receptor clients (Grad and Picard, 2007; Pratt and Toft, 1997), and have distinct functions in potentiating ligand binding and nuclear localization (Riggs et al., 2003; Storer et al., 2011; Wochnik et al., 2005). Notably, FKBP51 was recently discovered to act on Cdk4 in the Hsp90-stabilized complex, revealing a key role for its PPIase activity in Cdk4 inhibition (Ruiz-Estevez et al., 2018). Additionally, Hsp90:FKBP51 interacts with Tau, increasing stability (Jinwal et al., 2010) and promoting neurotoxic accumulation in neurodegenerative disease pathways (Blair et al., 2013).

How FKBP51 recognizes and acts on Hsp90-bound clients is unknown. Hsp90 exists as a homodimer through a C-terminal domain (CTD) interface and undergoes large, nucleotide-specific conformational changes during its chaperone cycle. The N-terminal ATPase domains (NTDs) dimerize upon ATP binding, forming a closed conformation that is activated for hydrolysis. The ability to form this closed, ATP state is rate limiting for hydrolysis (Prodromou et al., 2000; Richter et al., 2008) and varies across homologs (Southworth and Agard, 2008). Cochaperones Aha1 and p23 recognize the closed state and competitively bind NTD-MD sites across the dimer, thereby promoting (Aha1) or inhibiting (p23) ATPase activity (Ali et al., 2006; Meyer et al., 2004; Schopf et al., 2017). The structure of the closed state Hsp90:Cdc37:Cdk4 complex reveals the kinase client is unfolded with its N-lobe threaded between the monomers, contacting hydrophobic substrate-binding sites in the MD (Verba et al., 2016). While biochemical studies establish FKBP51 functions with p23 during client maturation (Ebong et al., 2016; Grad and Picard, 2007; Ni et al., 2010), recent NMR studies indicate FKBP51 stabilizes the Hsp90 open state to facilitate Tau binding (Oroz et al., 2018).

Here we sought to determine the structural basis for FKBP51 interaction with Hsp90 during the nucleotide-dependent chaperone cycle. Focusing on human FKBP51, p23 and Hsp90α,

we developed *in vitro* conditions that promote and stabilize the closed, ATP conformation of Hsp90, enabling characterization of binding interactions between the defined states. We identify that FKBP51 preferentially binds the closed, ATP state, forming a complex with a 2:1 stoichiometry that is further stabilized by p23 binding. By cryo-EM we determined a 3.3 Å structure of the Hsp90:FKBP51:p23 complex that reveals distinct contacts by FKBP51 and define its asymmetric interaction and recognition of Hsp90. Photocrosslinking and mutagenesis further establish key interactions by the FK1 and TPR domains. From these results we propose a model in which helix 7 (H7) of the TPR domain functions as a critical specificity element for engaging Hsp90 in the ATP state and enabling the PPIase-active FK1 domain to be positioned adjacent Hsp90 client binding sites to promote client re-folding and maturation.

Results

FKBP51 preferentially recognizes the closed Hsp90 conformation.

Immunophilins are present with p23 in Hsp90-steroid hormone receptor maturation complexes (Ebong et al., 2016; Johnson and Toft, 1994; Nair et al., 1997). While FKBP51 interaction with the Hsp90 open state has been characterized previously (Oroz et al., 2018), we hypothesized that the interactions may differ between the open (apo) and closed (ATP) Hsp90 conformations. Unlike *E. coli* and yeast homologs, human Hsp90 favors the open conformation even when bound to the nonhydrolyzable ATP analog, AMPPNP *in vitro* (Southworth and Agard, 2008). Therefore, reaction conditions including nucleotide (AMPPNP), temperature (0°C, 25°C, and 37°C) and salt concentration (10, 50, 250, and 500 mM KCl) were investigated for stabilizing the closed state of human Hsp90α (Figure S1A). By native gel two distinct mobilities for Hsp90 are identified under these conditions. In low salt or temperature or in the absence of AMPPNP a slower-migrating band is primarily observed, which likely corresponds to the open conformation (Figure 1A). A faster-migrating band appears following incubation in high salt (500 mM) and temperature (37 °C) with AMPPNP. This band likely corresponds to the closed conformation based on this increased mobility and dependence on AMPPNP. Notably, based on these data, both high temperature and salt concentration are required along with AMPPNP in order to promote a complete mobility shift (Figure 1A and S1A). Only a minor amount of the higher mobility band is observed at 25°C or in moderate salt concentrations (10–50mM), further supporting the high (37°C) temperature and salt dependence (Figure S1A). Additionally, an increase in this species is observed with $(NH_4)_2SO_4$ compared to NaCl and KCl, indicating salts that are more kosmotropic may be favorable (Figure S1B).

Hsp90 conformations were additionally characterized by size-exclusion chromatography coupled to multiangle light scattering (SEC-MALS) (Figure 1B). Apo Hsp90 elutes at ~8.8 ml (black) with an average molecular weight (mw_{avg}) of 174 kDa, indicating a dimer species based on its calculated molecular weight (mw_{calc}) of 169 kDa. Following incubation with AMPPNP at 37°C in high salt (500 mM KCl) the Hsp90 elution peak shifted to ~9.0 ml (red), while the mw_{avg} remained similar (172 kDa), indicating a conformational change to a more compact dimer state. As with the native gel analysis, incubation at a lower temperature (green) or lower salt concentration (blue) resulted in only slight shifts in the elution profile,

indicating both higher temperature and salt concentration promote this nucleotide-dependent conformational change. The Hsp90 conformation was verified directly by negative-stain EM (Figure 1C and S1C). In the absence of AMPPNP, Hsp90 particles adopt an open, extended conformation reflective of the apo state, similar to previous studies (Southworth and Agard, 2008). Conversely, analysis of Hsp90 incubated with AMPPNP and high salt at 37°C reveals the particles shift to a closed conformation which matches the NTD-dimerized, ATP state (Ali et al., 2006; Verba et al., 2016). Together, these results reveal that for nucleotide-bound human Hsp90α, high ionic strength and temperature together promote formation of the closed, ATP state.

Next, interaction between FKBP51 and Hsp90 in the open and closed states was characterized by SEC-MALS. Incubations were performed in the presence of 500 mM KCl at 37°C with and without AMPPNP. For Hsp90 incubated with FKBP51 in the absence of nucleotide the predominant peak elutes at ~8.8 ml with a mw_{avg} of 180 kDa which is slightly higher than apo Hsp90 alone, indicating potentially weak binding of FKBP51 (Figure 2A). Strikingly, incubation of Hsp90 and FKBP51 with AMPPNP under the closed state conditions resulted in peak elution at ~8.9 ml and a mw_{avg} of 218 kDa (Figure 2A). This is a shift by ~0.1 ml and an increase in mw_{avg} by 46 kDa compared to the closed state Hsp90, indicating formation of an Hsp90:FKBP51 complex with an approximately 2:1 stoichiometry, based on the mw_{calc} of 51 kDa for FKBP51. Analysis of the peak fractions revealed Hsp90 and FKBP51 co-elute in this peak, with AMPPNP, while a minor amount of FKBP51 is present in the absence of AMPPNP (Figure S2A and S2B). These results therefore indicate that FKBP51 more stably binds the closed, ATP conformation of Hsp90, forming a 2:1 asymmetric complex.

Interaction with the p23 cochaperone was tested to determine compatibility with the Hsp90:FKBP51 closed-state complex. For apo Hsp90, the elution and mw_{avg} did not change substantially following incubation with p23, while a modest increase in the mw_{avg} to 183 kDa was identified under closed-state conditions with AMPPNP, indicating partial p23 binding (Figure 2B). By gel analysis of fractions from SEC, p23 co-elutes with the closed state Hsp90 but is not present in the apo Hsp90 fractions, indicating preferential binding to the closed state (Figure S2A and S2C). Thus, while the interaction appears to be low affinity with a possible 2:1 stoichiometry, this supports the known p23-specificity for the closed, ATP state of Hsp90 (Richter et al., 2004; Siligardi et al., 2004). When p23 was next incubated with Hsp90 and FKBP51 under the closed-state conditions the mw_{avg} increased to 225 compared to 172 and 218 kDa for Hsp90 alone or with FKBP51, respectively (Figure 2C). Both p23 and FKBP51 co-elute with the closed-state Hsp90 in these fractions, indicating formation of a ternary complex with FKBP51 (Figure S2A and S2D). The calculated mw for an Hp90:FKBP51:p23 complex with one or two bound p23 molecules is 240 and 260 kDa, respectively. While a 2:1:1 stoichiometry more closely matches the mw_{avg}, the lower value indicates there is likely partial or mixed occupancy under these conditions. No substantial changes in elution or mw_{avg} were observed under apo-state conditions compared to Hsp90 incubated with FKBP51 (Figure 2A and 2C). Together these results indicate that FKBP51 preferentially recognizes the closed, ATP state of Hsp90, binding asymmetrically with a 2:1 stoichiometry. Moreover, this interaction is compatible with p23 binding, resulting in the formation of a ternary, client-maturation complex.

Cryo-EM structure of the Hsp90:FKBP51:p23 complex

We next performed cryo-EM to determine the structural basis of the Hsp90:FKBP51:p23 interaction. Initial screening by cryo-EM indicated the complex is unstable, likely due to the vitrification conditions. Therefore, in order to improve stability and occupancy of FKBP51, samples were diluted and crosslinked by low-level (0.01%) glutaraldehyde crosslinking in 100 mM KCl after the complex formation (Southworth and Agard, 2011). The 2D class averages of crosslinked Hsp90:FKBP51:p23 appear homogenous, exhibiting the closed-state architecture of Hsp90, but with additional density extending from CTD region (Figure 3A and S3A).

Following 3D classification and refinement a final map at 3.3 Å overall estimated resolution was achieved containing well-resolved density for the Hsp90 dimer and singly-bound FKBP51 and p23, revealing an asymmetric 2:1:1 arrangement (Figure 3B, S3B Class 2–3, S3C and Video S1). Particle orientations are well-distributed with some preferred side-views (Figure S3D). Hsp90 adopts the canonical two-fold symmetric closed state conformation in which dimeric interactions occur in both NTDs and CTDs. The Hsp90 dimer is at a higher resolution (< 3.0 Å) while density for FKBP51 and p23 is lower (5–8 Å and 3–6 Å, respectively), indicating flexibility or reduced occupancy (Figure S3E). Nonetheless, density for all three FKBP51 domains is identified, with strong density for the TPR α-helical bundle adjacent the Hsp90 CTD and weaker density for the FK1 and FK2 domains present along the MD of one monomer (Figure 3B). Density corresponding to one p23 molecule is present on the opposite side of Hsp90, interacting at the cleft between the two NTDs (Figure 3B).

The reconstruction was sufficient to build a molecular model of the Hsp90:FKBP51:p23 ternary complex by rigid-body docking homology models from existing structures and refinement with Rosetta (Figure 3C and S3F) (Kumar et al., 2017; Song et al., 2013; Verba et al., 2016; Weaver et al., 2000). The model for the Hsp90 dimer is similar to previous structures of yeast (Ali et al., 2006) and human (Verba et al., 2016) Hsp90 in the closed, ATP state (Cα-r.m.s.d. = 1.6 Å and 1.1 Å, respectively). NTD dimerization is defined by symmetric β-strand strap interactions across the top of the NTDs (residues 17–25), and the subsequent αH1 segment, which interacts across the dimer interface (Figure S4A, top-left). Similar to other ATP-state structures, the α-helical lid segment (residues 109–139) closes across the nucleotide pocket in both monomers and R400 in the MD contacts γ-phosphate of AMPPNP, forming the canonical Arg-finger interaction, which stabilizes the closed conformation required for hydrolysis (Figure S4A, top-right) (Ali et al., 2006; Cunningham et al., 2012). Additionally, MD amphipathic loops (residues 349–359 and residues 617–621) involved in substrate binding protrude into the dimer cleft (Figure S4A, bottom-left), and the CTDs interact primarily via hydrophobic contacts by the last two α-helices (αH17 and αH18, residues 657–695), which are essential for dimerization and hydrolysis (Figure S4A, bottom-right) (Minami et al., 1994; Prodromou et al., 2000).

FKBP51 fits unambiguously into the density and adopts a similar overall conformation as the crystal structure except for rotations around the FK2-TPR linker (Figure 3B and 3C) (Kumar et al., 2017). The majority of interaction with Hsp90 occurs through the TPR domain, which makes multiple surface contacts with the CTD (Figure 3C, discussed below). Notably, the FK1 domain makes minor contact with Hsp90 along the MD adjacent

the substrate-binding loops. While p23 interacts with Hsp90 NTDs on the opposite dimer interface, the position of FKBP51 does not appear to overlap directly with where p23 could bind on the same side. Indeed, we identify partial density for p23 on the same side of Hsp90 as FKBP51 in one of the 3D classes (Class 2–1) (Figure S3B and S4B). Thus, p23 may be able to interact adjacent FKBP51 on the same side in certain client maturation complexes.

Additionally, one 3D class (Class 1–1) exhibited well-defined density for a single p23 but no density for FKBP51 (Figure S3B), while two other classes (Class 2–2 and 2–4) contained a single FKBP51 but no p23. Classes 2–2 and 2–4 did not improve with refinement. Class 1–1 refined to 3.1 Å with improved resolution for p23 compared to the full complex (Figure S3C–F). The atomic model determined for Hsp90:p23 (Figure S4C) is similar to yeast Hsp90:p23 (Ali et al., 2006) (Figures S4D) and the recent structure of human GR:Hsp90:p23 (Noddings et al., 2020) as well as Hsp90:FKBP51:P23 (Cα-r.m.s.d. of 0.3 Å), determined here. Key Hsp90-p23 interactions include contacts by conserved hydrophobic residues F103 and W106 of p23 with a hydrophobic pocket (residues L335, L394, P395, I408 and V411) in the MD of Hsp90 (Figure S4D, bottom-left). K95 of p23 appears to form a salt bridge with E336 in the MD of Hsp90 and N97 (P115 in yeast) contacts M199, L122 and N123 in the lid of Hsp90, likely stabilizing the closed conformation (Figure S4D, top-left). Additionally, conserved residues R71 and D70 of p23 appear to interact with Hsp90 S31, A166 and S165 (Figure S4D, top-right).

Hsp90:FKBP51 interactions are defined by contact between the Hsp90 CTD and the TPR helix 7 extension

In the Hsp90:FKBP51:p23 structure the TPR domain of FKBP51 is oriented with the MEEVD binding pocket positioned away from the Hsp90 CTD (Figure 4A). Additional density is identified in this pocket and a DTSRMEEVD peptide docks appropriately into the density based on previous crystal structures (Figure 4A) (Kumar et al., 2017). However, the resolution was not sufficient to confirm the sequence. This peptide connects to the Hsp90 CTD by ~30-residue linker which is not visible, but likely sufficient to span the ~40 Å needed to reach the last C-terminal residues (I698) resolved in the structure at the base of the CTD (Figure 4A, right). Thus, FKBP51 appears engaged with one MEEVD of Hsp90, however, the peptide may be derived from either monomer.

Surprisingly, the C-terminal H7 extension (H7e) of the FKBP51 TPR forms a distinct kinked conformation compared to crystal structures (Kumar et al., 2017; Sinars et al., 2003), and interacts directly with the Hsp90 CTD dimer (Figure 4B and S5A–C). H7e projects across the base of Hsp90, contacting both monomers in a hydrophobic cleft at the dimer interface comprised of the last two CTD helices (αH17 and αH18) (Figure 4C). Notably, the H7e helix residues 409–413 are distorted, enabling H7e to match the bend in the CTD cleft at the two-fold axis and contact both monomers (Figure S5A–C). Overall, the H7e region buries ~830 $Å^2$ of CTD surface area, which is larger than what is estimated for MEEVD interaction (~500 $Å^2$) (Kumar et al., 2017), thus revealing a new and substantial binding interface beyond the canonical TPR interaction.

This helix is well-resolved and distinct side-chain contacts with Hsp90 are identified (Figure 4B). Hydrophobic residues I408, Y409, M412, F413 and F416 in the unfolded strand of

H7e interact with Hsp90 CTD residues 691–696, which together form distinct hydrophobic cleft between the C-terminal helices (αH17 and αH18) of each Hsp90 monomer (Figure 4C). Flanking this interaction, R690 from each Hsp90 monomer appear to make salt-bridge contacts with D405 and D420 in H7e on either side of the hydrophobic residues (Figure 4B). Additional contacts with Hsp90 occur between the H5-H6 connecting strand in FKBP51, including N365, which appears to make backbone contact with N655 in Hsp90 (Figure S5D). Overall, the H7e-CTD interaction appears to be a significant component of the Hsp90:FKBP51 maturation complex and the position enables H7e to make symmetrical contact across the CTD dimer, thereby precluding the binding of two FKBP51 molecules.

Next, we sought to characterize the significance of H7e in Hsp90 binding by mutagenesis and SEC-MALS analysis. Truncation of H7e from position H401 (ΔH7e) substantially reduced FKBP51 binding to Hsp90 under closed-state conditions, as indicated by the decrease mw_{avg} from 218 kDa to 188 kDa and shift in elution volume (Figure 4D and 4F). No substantial changes were observed under Hsp90 open-state conditions; both wt and ΔH7e exhibit incomplete binding to apo Hsp90 (Figure S5E). To test the significance of the hydrophobic interactions with the CTD cleft, mutations M412K and F413K were tested. N402K was included as a control due to its position outside the CTD interaction site, based on the structure. For M412K and F413K, the mw_{avg} is substantially reduced (186 kDa and 184 kDa, respectively) compared to the wt complex, and the elution volume overlaps with Hsp90 alone, indicating loss of FKBP51 binding (Figure 4E and 4F). The N402K mutation exhibits no significant change in the mw_{avg} and elution volume compared to the wt complex, validating that this site does not participate in Hsp90 binding. Together, these results establish that H7e is critical for FKBP51 binding to Hsp90. Moreover, the hydrophobic contacts with the Hsp90 C-terminal helices identified in the structure, involving the 408–416 unfolded strand, indeed appear to coordinate this interaction. The H7e itself, as well as residues Y409, M412, and F413 are conserved among the immunophilin-class of TPR cochaperones (Figure S5F). Thus, the interaction identified here likely represents a conserved Hsp90-specific recognition mechanism for these cochaperones.

In order to further characterize the Hsp90-FKBP51 interaction, competition fluorescence polarization (FP) experiments were conducted, as previously described (Assimon et al., 2015; Ravalin et al., 2019), using a fluorescently labeled peptide tracer corresponding to the extreme C-terminus of Hsp90α (FAM-DDTSRMEEVD). For these experiments we postulated that Hsp90 in the closed state would compete off the peptide tracer and bind FKBP51 at a lower concentration compared to the open state, indicating a higher affinity interaction (Figure S6A). Saturation binding of the tracer to FKBP51 wt and ΔH7e revealed similar affinities (K_d = 3.3 μM and 4.4 μM, respectively), indicating deletion of H7e does not alter binding of the EEVD peptide to the TPR domain of FKBP51 (Figure S6B). In competition experiments, closed-state Hsp90 inhibited tracer binding to wt FKBP51 with an IC_{50} of 3.8 μM (Figure 4G). Conversely, an IC_{50} of 10.2 μM was determined for Hsp90 in the open state. From these experiments, Ki values were determined to be 0.9 and 3.0 μM for the closed and open states, respectively, revealing a ~3.3-fold increase in affinity when Hsp90 is in the closed-state conformation (Figure 4I). Remarkably, this is identified through competition for the TPR binding pocket by the Hsp90 EEVD, which is at the end of a flexible C-terminal tail and expected to be fully accessible in both the open and closed

states. This indicates that the binding discrimination likely comes from other interactions between Hsp90 and FKBP51, such as the H7e interaction that we identified in the structure. When binding was next tested with the FKBP51 ΔH7e we identified a substantially weaker competitive interaction and no differences between the closed and open states (IC_{50} = 18.3 and 13.6 μM, respectively), indicating that removal of the H7e results in a loss of discrimination between the closed and open Hsp90 states (Figure 4H). These results are in agreement with the SEC-MALS data and establish that FKBP51 has a higher affinity for Hsp90 in the closed, ATP compared to open state. Furthermore, the H7e interaction indeed functions as a key component of the Hsp90 closed-state interaction.

H7e binding specificity to the Hsp90 CTD dimer in the closed state

In order to understand the H7e interaction further, the CTD dimer conformation was compared between the open and closed states, based on structures of apo Hsp90 (*E. coli* HtpG) (Shiau et al., 2006) and Hsp90:FKBP51:p23, determined here (Figure 5). Notably, the Hsp90 structure and sequence is highly conserved across species (39% sequence identity and 59% sequence similarity between *E. coli* HtpG and human Hsp90α). By global alignment (Cα) the CTD conformation does not vary substantially between the open and closed states (r.m.s.d = 1.8 Å) (Figure S6C). However, comparison of the CTD dimer interface reveals CT-helices αH17 and αH18 undergo distinct conformational changes that widen the CTD cleft from ~6 to 12Å, thereby enabling the hydrophobic groove to become more accessible in the closed state (Figure 5A and Video S2). By modeling H7e across the CTD in the apo state, residues M412 and F413 appear to clash with Hsp90 residues L662, M691, and L694, indicating the CTD may be incompatible for binding in this state (Figure 4C and 5B). In addition, changes in the CTD would shift αH17, bringing it closer to TPR helices H5 and H6 of FKBP51, likely altering interactions with FKBP51 N365 (Figure 5B and S5D). Based on these comparisons, the Hsp90 CTD dimer interface involving αH17 and αH18 undergoes conformational changes from the open to closed states that likely result in improved accommodation of the H7e strand, thereby specifying FKBP51-binding to the closed state of Hsp90.

Position of the FK1 domain supports PPIase-directed activity on Hsp90-bound clients

In the Hsp90:FKBP51:p23 structure FKBP51 extends from the CTD-TPR interaction along the Hsp90 MD, enabling the N-terminal FK1 domain to be positioned adjacent Hsp90 client interaction sites (Figure 6A, bottom) (Genest et al., 2013; Verba et al., 2016). The FK1 PPIase active site is comprised of a series of β strands that form a conserved hydrophobic pocket where immunosuppressive drugs bind, including FK506 and rapamycin (Hahle et al., 2019). This pocket is approximately 17 Å from Hsp90 client binding sites, which include Y528, Q531, and M610 (Genest et al., 2013), and have been identified to contact the unfolded Cdk4 client in the Hsp90:Cdc37:Cdk4 closed state structure (Verba et al., 2016). In order to further characterize the proximity of the FK1 domain to Hsp90, site specific crosslinking was performed by incorporating the photoactivatable unnatural amino acid, p-benzoyl-l-phenylalanine (Bpa) into specific positions in FKBP51. A bulge within the β3 strand is the closest to the Hsp90 client biding site (~5 Å away) and was thus chosen for Bpa incorporation (Figure 6A, top). Bpa was incorporated into D72, N74, and E75 and full-length protein was purified and crosslinked with Hsp90 under closed and open-state

conditions (Figure 6B). By SDS-PAGE, distinct high-mw bands are identified for all 3 sites only in the presence of Hsp90 and following UV exposure, confirming that FKBP51 β3 is indeed in close proximity to Hsp90. Notably for D72Bpa, strong crosslinked bands are only present under the Hsp90-closed state condition, indicating that crosslinking at this position is conformation-specific. Additionally, N74Bpa and E75Bpa each show crosslinked-bands under open-state conditions, however, these bands diminish for the closed state, while several other bands appear, revealing distinct interactions in the open and closed states. In contrast, we observe no or very minimal crosslinking products for Bpa incorporated at sites (E23, S27, and K29) on the opposite side in the FK1 domain that are predicted to be distal from Hsp90 based on our model (Figure S7A–C). Thus, Bpa incorporation at this β3-strand bulge position provides a crosslinking-readout for the Hsp90 conformation and confirms the FKBP51-specificity for the Hsp90 closed state and positioning of FK1 PPIase site adjacent Hsp90. Based on the close proximity of the PPIase site to the Hsp90 client binding strands we predict that FKPB51 may target specific client proline residues near where Hsp90 binds clients. Furthermore, the position of the β3-strand bulge is intriguing and may provide an important interaction link with Hsp90 to facilitate client positioning for chaperone activation.

Discussion

FKBP51 has been proposed to act during client maturation, but the structural basis for how the TPR-containing cochaperone recognizes Hsp90 or is positioned for client interactions has been unclear. Here we identified that FKBP51 preferentially binds Hsp90 in the closed, ATP state and determined a structure of the Hsp90:FKBP51:p23 complex, revealing the basis for FKBP51 recognition of this conformation. With these findings we propose a model in which FKBP51 acts specifically during the client maturation step, binding Hsp90 in the ATP-bound state following client loading and NTD dimerization (Figure 6C). In agreement with this model, recent work identifies that Hsp90-GR client-bound complexes form the closed state cooperatively with the binding of FKBPs (Kaziales et al., 2020). The Hsp90:FKBP51:p23 structure reveals that the TPR H7e from FKBP51 binds across a hydrophobic groove in the Hsp90 CTD dimer, which appears distinctly accessible in the closed state compared to the apo Hsp90 CTD (Figure 4 and 5). Interactions by the TPR with the Hsp90 CTD enable FKBP51 to extend along the Hsp90 MD with its PPIase-active FK1 domain positioned adjacent Hsp90 client binding loops, potentially enabling FKBP51 catalytic activity to be directed at specific proline residues in the bound client. Alternatively, for certain clients such as GR, the FK1 domain may instead be positioned to interact with clients or provide scaffolding functions that promote activation independently of prolyl isomerization (Riggs et al., 2007).

Cryo-EM structures of the client-bound Hsp90 reveal the client undergoes substantial unfolding, likely upon formation of the Hsp90 closed state (Noddings et al., 2020; Verba et al., 2016). The N-lobe of Cdk4 is unfolded and threaded though the MD dimer cleft in the Hsp90:Cdc37:Cdk4 structure exposing a strand of residues that would be inaccessible in the folded state (Verba et al., 2016). Based on this arrangement, the position of the FK1 domain in our structure appears positioned for catalyzing isomerization of proline residues localized in unfolded regions or adjacent sites that are optimally presented in the Hsp90-bound state

of the client. Moreover, FKBP51 interaction may then accelerate client folding on Hsp90 or stabilize an activated state that is competent for ligand binding or other downstream function. Indeed, modeling of Cdk4 into the Hsp90:FKBP51:p23 structure reveals that P173, a recently-identified FKBP51 target (Ruiz-Estevez et al., 2018), docks into the FK1 active site following minor conformational changes (Figure S7D). The flexibility of the FK1 domain likely enables FKBP51 to engage slightly different client positions on Hsp90 while maintaining TPR interactions, including H7e contact with the CTD.

Hsp90:FKBP51 functions in tau proteostasis, increasing its stability and altering phosphorylation states (Blair et al., 2013; Jinwal et al., 2010). By NMR, Hsp90 is identified to interact with tau transiently in the apo state and function as a scaffold in complex with FKBP51 (Karagoz et al., 2014; Oroz et al., 2018). While Hsp90-FKBP51 contacts we identify appear similar to CTD and MD interaction regions identified by NMR, we observe only weak binding to the apo state by SEC and FP. Additionally, contrary to the apo state interaction, our data and cryo-EM structure establish that Hsp90 binds FKBP51 with a specific 2:1 stoichiometry in the closed state that is defined by the H7e binding across the CTD dimer interface. Given this binding groove can only accommodate a single H7e, our structure therefore excludes possibility that a tetramer with two FKBPs can occur in this arrangement. Moreover, in the apo state the CTD dimer cleft has reduced accessibility and may be incompatible for H7e binding. While engagement by the H7e may induce widening of the CTD, enabling its accommodation, in existing closed state structures (Huck et al., 2017; Verba et al., 2016) the CTD adopts this widened conformation in the absence of a bound H7e moiety, indicating this may result from NTD dimerization alone.

The residues in H7e identified to contact the Hsp90 CTD groove (notably Y409, M412, and F413) are conserved among TPR-containing PPIase cochaperones (FKBP51, FKBP52, FKBP36, FKBP38 and Cyp40) and part of a region previously designated as the ‘Charge-Y’ motif that was shown to be important for Hsp90 binding (Figure S5F) (Cheung-Flynn et al., 2003). FKBP51/52 are highly similar in their structure and sequence (60% sequence identity) (Wu et al., 2004). Both are found in GR maturation complexes and appear to have opposing roles in dynein-mediated nuclear localization (Grad and Picard, 2007; Wochnik et al., 2005). Only minor differences between FKBP52 and FKBP51 are identified in the crystal structures due to changes in the FK2-TPR domain orientation (Hahle et al., 2019; Wu et al., 2004). This could lead to different positioning of the FK1 domain when bound to Hsp90. However, the FK domains are connected by linkers and based on the cryo-EM density, appear flexible when bound to Hsp90. Thus, we postulate that the organization of FKBP51/52 on Hsp90 is highly similar but with modestly different positioning of the FK1 domains that may be further specified by additional client and cochaperone interactions. Indeed, the proline-rich loop (residues 116–124) in of FKBP51 and FKBP52 is proposed to recognize different conformations of GR in regulating steroid hormone binding (Riggs et al., 2007) and may contribute to conformational differences. Conversely, Cyp40 and FKBP38 are more structurally diverse, containing single FK-like or Cyp (cyclosporin-binding) PPIase domain, respectively, and therefore likely interact differently with Hsp90. Nonetheless, based on the well-defined TPR contacts we identify, Hsp90 interactions with the PPIase cochaperones are expected to be largely conserved and defined by the TPR-CTD interaction.

The Hsp90-p23 contacts are largely conserved between yeast and human Hsp90 systems. However, unlike the crystal structure of yeast Hsp90:p23, the structures presented here (Hsp90:FKBP51:23 and Hsp90:p23) as well as the recent cryo-EM structure of GR:Hsp90:p23 (Noddings et al., 2020), indicate a single p23 molecule appears to bind the human Hsp90 dimer in the maturation state. In our classification and refinements, density for p23 appears on the opposite side of Hsp90 from FKBP51. However, the FKBP51 interaction site does not overlap substantially, indicating p23 binding may only slightly favor the opposite NTD interface and in one class partial density for p23 was resolved on the same side as FKBP51 (Figure S4B). In the GR:Hsp90:p23 structure (Noddings et al., 2020), p23 directly contacts the GR client and enhances ligand binding via its C-terminal tail helix, which is unresolved in our structures. Thus, the positioning of p23 and FKBP51 are likely further specified by interactions with the bound client.

The TPR:EEVD interaction is known to provide the majority of binding energy for Hsp70/Hsp90:cochaperone complexes, enabling cochaperones such as PP5, Hop and CHIP to function in both Hsp70 and Hsp90 pathways (Assimon et al., 2015; Connarn et al., 2014; Scheufler et al., 2000; Smith et al., 2013). Based on our SEC-MALS and FP data we do identify binding between FKBP51 and Hsp90 in the open state, but with a substantially lower affinity. This may reflect TPR-EEVD binding is occurring without engagement of H7e, as indicated by experiments with ΔH7e in which Hsp90-FKBP51 interactions are weaker and no longer specific to the closed state (Figure 4H). Thus, initial TPR-EEVD binding may occur in the open state and promote Hsp90 conformational changes that enable engagement by H7e and conversion to the closed, client-maturation state. The ~30 residue linker connecting the EEVD to the Hsp90 CTD is not resolved in the Hsp90:FKBP51:p23 structure, indicating these residues do not contribute to FKBP51 binding. Hsp70 similarly contains an unstructured EEVD-connecting linker that may not participate directly in cochaperone interactions (Zhang et al., 2015). These linkers may instead primarily function to enable TPR-cochaperones to be positioned at different binding sites on Hsp90 or Hsp70 in facilitating their diverse functions.

Our mutagenesis data of H7e indicate this element is critical for Hsp90 binding, and the TPR:EEVD interaction alone is insufficient for stable formation of the complex (Figure 4). These data, together with structure identifying the H7e-CTD interaction, reveal that the H7e functions as a key recognition element that enables FKBP51 to bind Hsp90 over Hsp70 and, further, interact specifically with the closed state conformation. Thus, these additional cochaperone:chaperone binding interfaces revealed in structures of intact complexes are likely necessary for enabling cochaperones to engage different steps of the chaperone cycle and client-folding states. Indeed, structures of Hsp90:Hop and, recently, GR:Hsp90:Hsp70:Hop identify that Hop stabilizes the Hsp90 client loading state and participates in client interactions, revealing an active role for Hop in the folding cycle beyond tethering Hsp70 and Hsp90 during client hand-off (Southworth and Agard, 2011; Wang et al., 2020).

Limitations of the study

Based on the work presented here and previous structures of Hsp90-client complexes (Verba et al., 2016; Noddings et al., 2020) we predict FKBP51 interacts directly with clients threaded through the lumen of Hsp90 in the closed, ATP state to promote client maturation. This may occur through contact by the FK1 domain and PPIase-directed activity at specific sites presented in the Hsp90-bound state. Alternatively, the FK1 domain may confer general protein folding or stability functions during the chaperone cycle. Thus, determining structures of the Hsp90:FKBP51:p23 complex bound to an unfolded client, such as GR, are an important future direction and would provide critical insight into the chaperone mechanism of FKBP51. Furthermore, structures of Hsp90 complexes with FKBP52, which is highly homologous to FKBP51, are of significant interest in order to identify the structural basis for the distinct cellular functions of these immunophilins (Riggs et al., 2007; Dickey et al., 2007; Jinwal et al., 2010).

STAR Methods

RESOURCE AVAILABILITY

Lead contact—Further information and requests for resources and reagents should be directed to and will be fulfilled by the Lead Contact, Daniel R. Sourthworth (daniel.southworth@ucsf.edu).

Materials Availability—Requests for resources and reagents should be directed to Daniel R. Sourthworth (daniel.southworth@ucsf.edu).

Data and code availability

- Cryo-EM densities have been deposited at the Electron Microscopy Data Bank under accession codes EMD: 23213 (Hsp90:FKBP51:p23 closed-state complex) and EMD: 23214 (Hsp90:p23 closed-state complex). Atomic coordinates have been deposited at the Protein Data Bank under accession codes PDB: 7L7I (Hsp90:FKBP51:p23 closed-state complex) and PDB: 7L7J (Hsp90:p23 closed-state complex).
- This paper does not report original code.
- Any additional information required to reanalyze the data reported in this paper is available from the lead contact upon request.

EXPERIMENTAL MODEL AND SUBJECT DETAILS

Bacterial strains—BL21-AI™ One Shot™ Chemically Competent *E. coli* or BL21 Star™ (DE3)pLysS One Shot™ Chemically Competent *E. coli* from Invitrogen were used to express recombinant proteins.

METHOD DETAILS

Protein expression and purification—NEB Q5 Site-directed Mutagenesis was used to introduce mutations (Deletion 401–457 (ΔH7e), N402K, M412K, and F413K) into

the open reading frame of FKBP51 in pET151 vector with a 6x His-tag and TEV cleavage site (Invitrogen). Hsp90, p23, FKBP51 and its mutants were purified as previously described with minor modifications (Southworth and Agard, 2008, 2011). *E. coli* BL21 cells were transformed with pET151-Hsp90α, pET151-p23, and pET151-FKBP51 plasmids, respectively. The cells were grown in Terrific Broth (TB) media at 37°C and induced with 1 mM IPTG at OD_{600} = 0.8 – 1.0 for overnight at 18°C after cooling on ice. The cells were lysed by either sonicator or Emulsiflex in the lysis buffer (20 mM Tris pH 8.0, 500 mM KCl, 6 mM β-mercaptoethanol, 3 mM imidazole, and 10% glycerol with EDTA-free protease inhibitor cocktail (Roche). The lysed cells were centrifuged with 40,000 rpm at 4°C for 45 min. The supernatant was incubated with HisPur Ni-NTA resin (Thermo Scientific) at 4°C for 1 hour. The resins were applied to a benchtop Ni-NTA column and bound proteins were eluted with an elution buffer (20 mM Tris pH 8.0, 100 mM KCl, 6 mM β-mercaptoethanol, and 300 mM imidazole) by gravity force. The eluted proteins were applied to ion exchange column (Mono Q 5/50 GL, GE Healthcare) and eluted with a gradient of ion exchange buffer A and B (A: 20 mM Tris pH 8.0, 20 mM KCl, and 6 mM β-mercaptoethanol; B: 20 mM Tris pH 8.0, 500 mM KCl, and 6 mM β-mercaptoethanol). The fraction containing proteins were dialyzed with a dialysis buffer (20 mM Tris pH 8.0, 100 mM KCl, 6 mM BME, and 10% glycerol) containing TEV protease to cleave the His tag at 4°C overnight. Dialyzed samples were applied to a size exclusion column (HiLoad Superdex-200 16/600 column, GE Healthcare) with a gel filtration buffer (20 mM Tris pH 7.5, 250 mM KCl, 6 mM β-mercaptoethanol). Protein fractions were collected and dialyzed with a storage buffer (20 mM HEPES pH 7.5, 50 mM KCl, 6 mM β-mercaptoethanol, and 10 % glycerol) at 4°C overnight. Dialyzed proteins were concentrated and frozen with liquid nitrogen for storage at −80°C. Purity of proteins was verified by SDS-PAGE.

Native gel electrophoresis—The formation of open (apo) and closed (ATP-bound) states of Hsp90 in different conditions (salt, temperature, and nucleotide as described in Figure 1A, S1A and S1B) were tested using native gel electrophoresis. 2 uM of Hsp90 was incubated with a buffer (20 mM HEPES pH 7.5, 5 mM $MgCl_2$, and 6 mM β-mercaptoethanol) in addition to the conditions described for 2 hours. Hsp90 was then mixed with 2x Native PAGE sample buffer (62.5 mM Tris-HCl, pH 6.8, 40% glycerol, and 0.01% bromophenol blue) and run on a native gel (handcasting Tris polyacrylamide gel without SDS) in a Native PAGE buffer (25 mM Tris pH 8.3 and 0.192 M glycine). The gel was stained with Coomassie Blue (Bio-Rad).

SEC-MALS and size exclusion chromatography—20 uM of Hsp90, FKBP51, and p23 were incubated with the binding buffer (20 mM HEPES pH 7.5, 500 mM KCl, 5 mM $MgCl_2$, and 6 mM β-mercaptoethanol) in the absence or presence of 2 mM AMPPNP at 37°C for 2 hours before injection into a size exclusion column (Shodex KW-804) connected to an in-line DAWN HELEOS MALS and Optilab rEX differential refractive index detectors (Wyatt Technology Corporation) with the running buffer (20 mM HEPES pH 7.5, 150 mM KCl, 5 mM $MgCl_2$, and 6 mM β-mercaptoethanol) at 4°C. Molecular weight of proteins and protein complexes were analyzed by the ASTRA V software package (Wyatt Technology Corporation). Superose 6 Increase 3.2/300 column (GE Healthcare Life Sciences) with

the running buffer (20 mM HEPES pH 7.5, 150 mM KCl, 5 mM $MgCl_2$, and 6 mM β-mercaptoethanol) at 4°C was used to analyze elution fractions by SDS-PAGE.

Fluorescence polarization assays—For the competition experiments, 40 nM of the C-terminal Hsp90α peptide tracer (FAM-DDTSRMEEVD) (Assimon et al., 2015) was incubated with 5 μM of FKBP51 wildtype or ΔH7e in the tracer buffer (20 mM HEPES pH 7.4, 150 mM KCl, 5 mM $MgCl_2$, and 0.002% Triton X-100). Hsp90 was incubated with the binding buffer (20 mM HEPES pH 7.5, 500 mM KCl, 5 mM $MgCl_2$, and 6 mM β-mercaptoethanol) in the presence or absence of 2 mM AMPPNP at 37C for 2 hours to form the closed or open state, respectively. Then, two-fold serial dilution of Hsp90 was prepared in the protein buffer (20 mM HEPES pH 7.4, 150 mM KCl, 5 mM $MgCl_2$, and 2 mM β-mercaptoethanol). 9 μl of Hsp90 serial dilution was mixed with 9 μl of the FKBP51 and tracer solution, and then the mixture was incubated at room temperature for 15 min in the dark before fluorescence polarization measurements were taken on a SpectraMax M5 plate reader. Raw polarization values (mP) were background subtracted, normalized to no-competitor control, and plotted relative to $\log_{10}$(Hsp90) (M). Curves were fit in GraphPad Prism 9.0 to the model [inhibitor] versus normalized response. IC_{50} values were calculated based on following equation:

$$Y = 100/(1 + X/IC_{50})$$

K_i values were calculated as previously described (Nikolovska-Coleska et al., 2004) using the equation:

$$K_i = [I]_{50}/([L]_{50}/K_d + [P]_0/K_d + 1)$$

To determine K_d of FKBP51 wildtype and ΔH7e for the Hsp90 tracer, two-fold serial dilution of FKBP51 wildtype or ΔH7e from 20 μM to 0.625 μM were incubated with 20 nM of the Hsp90 tracer in the fluorescent polarization buffer (20 mM HEPES pH 7.4, 150 mM KCl, 5 mM $MgCl_2$, 0.001% Triton X-100, and 1 mM β-mercaptoethanol) for 15 min at room temperature in the dark. Raw polarization values (mP) were background subtracted and plotted relative to [FKBP51] (μM). Curves were fit in GraphPad Prism 9.0 using the model [agonist] versus response. K_d was extrapolated from half-maximal effective concentration (EC_{50}) using the equation:

$$Y = \text{Bottom} + (\text{Top} - \text{Bottom})/\left(1 + 10^{((\log EC_{50} - X) \times \text{HillSlope})}\right)$$

Bpa (p-bnezoyl-L-phenylalanine) crosslinking—*E. coli* cells were transformed with plasmids containing a TAG stop codon at specific sites (E23, S27, K29, D72, N74, and E75) of FKBP51 to incorporate Bpa by nonsense-suppression during translation in addition to Bpa-tRNA vector (pSUPT/BpF), encoding tRNA and tRNA synthetase, as describe previously (Lennon et al., 2012; Ryu and Schultz, 2006). The cells containing the plasmids were grown in the TB media supplemented with 1 mM of Bpa at 37°C until OD_{600} reached about 0.8–1. The cells were induced with 1mM of IPTG and 200 mg/L arabinose overnight

at 18°C. The cells were lysed with sonicator with lysis buffer (20 mM HEPES pH 7.5, 100 mM KCl, 5 mM $MgCl_2$, 6 mM β-mercaptoethanol, and 10 mM imidazole) and incubated with HisPur Ni-NTA resin (Thermo Scientific) for 1 hour at 4°C. Bound proteins were eluted with elution buffer (20 mM HEPES pH 7.5, 100 mM KCl, 5 mM $MgCl_2$, 6 mM β-mercaptoethanol, and 300 mM imidazole) and used for crosslinking. The open and closed states of Hsp90 were formed by incubation with the binding buffer (20 mM HEPES pH 7.5, 500 mM KCl, 5 mM $MgCl_2$, and 6 mM β-mercaptoethanol) in the absence or presence of 2 mM AMPPNP at 37°C for 2 hours. FKBP51 were mixed with Hsp90 in the open and closed states, respectively, and exposed to UV lights for 1 hours. Crosslinking was analyzed by SDS-PAGE.

Electron Microscopy (EM) data collection and processing—For negative-stain EM Hsp90 was incubated with the binding buffer (20 mM HEPES pH 7.5, 500 mM KCl, 5 mM $MgCl_2$, and 6 mM β-mercaptoethanol) in the presence or absence of 2 mM AMPPNP at 37°C to form the open and closed states, respectively. Hsp90 sampled at different incubation time points (0.5, 1, and 2 hours) was stained with uranyl formate for 30 seconds on carbon coated 400 mesh copper grids. The samples were imaged using a FEI Tecnai 10 operated at 100 keV. Micrograph images were recorded using a 4k × 4k CCD camera (Gatan).

For cryo-EM Hsp90α, FKBP51, and p23 were incubated with binding buffer (20 mM HEPES pH 7.5, 500 mM KCl, 5 mM $MgCl_2$, and 6 mM β-mercaptoethanol) at 37°C for 2 hours. After incubation the sample was diluted and crosslinked with 0.01% glutaraldehyde for 30 min in 100 mM KCl. The crosslinked sample was applied on a glow-discharged holey carbon grid (R 1.2/1.3, Quantifoil) after quenching with 20 mM Tris (pH 7.5) and blotted with Whatman filter paper before plunge freezing in liquid ethane using a vitrobot (ThermoFisher Scientific). The sample was then imaged on a Titan Krios TEM (ThermoFisher Scientific) operated at 300 keV equipped with a Gatan BioQuantum imaging energy filter using a 20-eV energy slit (Gatan). Micrograph images were recorded on a K2 Summit and K3 direct electron detector (Gatan) at a magnification of x61,425 and x58,600 which corresponds to a physical pixel sizes of 0.814 and 0.834 Å/pixel, respectively. Serial-EM was used to collect data with a defocus range of −2.0 to −1.0 um at a dose rate of 6 (K2) and 8 (K3) e^-/pix/s for total 8 and 6 seconds exposures at 0.05 s/frame in 120 frames resulting in total doses of 70 and 66 $e^-/Å^2$, respectively. Movies of images were corrected for drift using MotionCor2 (Zheng et al., 2017) and were Fourier cropped by a factor of 2. Micrographs were rescaled to be combined with other datasets using relion_image_handler as described previously (Scheres, 2012; Wilkinson et al., 2019).

A total of ~22,000 micrographs were collected from three different dataset. Individual micrographs were manually curated using Scipion (de la Rosa-Trevin et al., 2016) to exclude poor quality micrographs and CTF was estimated using Patch CTF in cryoSPARC2 (Punjani et al., 2017). cryoSPARC2 v3.1.0 with standard parameters was used throughout the data processing. About 100 particles were picked to generate templates which were then used for automated particle picking for each dataset. The first round of reference-free 2D classification was conducted with the particles which were autopicked and extracted from each dataset separately. The 2D class averages with high resolution features were selected, removing noisy or indiscernible class averages, and combined with the other data sets for

the second round of reference-free 2D classification. Three ab-initio models were generated with selected particles (~576,000 from about 3.6 million total picked particles) and used for subsequent 3D classification. For Hsp90:FKBP51:p23, initial 3D heterogeneous refinement was performed with three different classes (Figure S3B). Two classes (total of ~337,000 particles) containing distinct density for FKBP51 were combined for another round of 3D heterogeneous refinement with four different classes. Finally, non-uniform refinement was performed for a class (~122,000 particles) containing discrete density for FKPB51 and p23. A class (~295,000 particles) only containing p23 after the first round of 3D classification was used for non-uniform refinement to obtain the Hsp90:p23 reconstruction. The final resolutions for Hsp90:FKBP51:p23 and Hsp90:p23 were 3.3Å and 3.1Å, respectively as determined by the “Gold Standard” Fourier Shell Correlation method (Henderson et al., 2012).

Molecular modeling—To build a model structure of the Hsp90:FKBP51:p23 complex, initial model of Hsp90α was generated by SWISS-MODEL (Waterhouse et al., 2018) using Hsp90β structure (PDB: 5FWK) (Verba et al., 2016) as a template. Hsp90, FKBP51 (PDB: 5NJX) (Kumar et al., 2017), and p23 (PDB: 1EJF) (Weaver et al., 2000) were docked into the Hsp90:FKBP51:p23 density using the UCSF Chimera (Pettersen et al., 2004) fit-in-map function. AMPPNP were generated by Phenix eLBOW (Afonine et al., 2018; Liebschner et al., 2019) and placed into the NBD of Hsp90 based on the crystal structures of mitochondrial Hsp90 in the closed state (PDB: 4IPE) (Lavery et al., 2014). Initially Rosetta comparative modeling (RosettaCM) (Song et al., 2013) was used to model Hsp90, FKBP51, and p23 according to the density. Homology model structures of Hsp90 (PDB: 5FWK, 2CG9, 2O1U, 4IPE, 2IOQ, and 4IVG), FKBP51 (PDB: 5OMP, 1P5Q, 2IF4, 4LAY, 5MGX, and 3O5D), and p23 (PDB: 1EJF, 2KMW, 2CG9, 1RL1, 2O30, and 2XCM) were determined by HHpred respectively and used to constrain model refinement in RosettaCM with template_weitght=0 and the initial model with template_weight=1. The lowest energy models were examined, and the models that best fit into the density were chosen. Rosetta enumerative sampling (RosettaES) (Frenz et al., 2017) was used to build some regions of Hsp90 de novo. The Hsp90 residues 122–133, 175–183, 345–360, and 617–622 were deleted and RosettaES was run with beam width of 32, respectively. The resulting models of Hps90, FKBP51, and p23 were refined by Rosetta Relax with the Hsp90:FKBP51:p23 and Hsp90:p23 density maps, respectively. The final models were manually inspected with minor modification using ISOLDE (Croll, 2018) in ChimeraX (Pettersen et al., 2021) and Coot (Casanal et al., 2020).

QUANTIFICATION AND STATISTICAL ANALYSIS

Quantification and statistical analysis are described in the figure legends and METHOD DETAILS when applicable. Error bars represent standard deviation. *$p < 0.5$, ns = no significance.

Supplementary Material

Refer to Web version on PubMed Central for supplementary material.

Acknowledgments

We thank K. Lopez, A. Rizo and D. Agard for feedback on the manuscript. We thank the UCSF cryoEM Facility for assistance with data collection. This work was supported by an Alzheimer's Association Research Fellowship (to K.L.), and NIH grants AG002132 and AG068125 (to D.R.S.).

References

Afonine PV, Poon BK, Read RJ, Sobolev OV, Terwilliger TC, Urzhumtsev A, and Adams PD (2018). Real-space refinement in PHENIX for cryo-EM and crystallography. Acta Crystallogr D Struct Biol 74, 531–544. [PubMed: 29872004]

Ali MM, Roe SM, Vaughan CK, Meyer P, Panaretou B, Piper PW, Prodromou C, and Pearl LH (2006). Crystal structure of an Hsp90-nucleotide-p23/Sba1 closed chaperone complex. Nature 440, 1013–1017. [PubMed: 16625188]

Assimon VA, Southworth DR, and Gestwicki JE (2015). Specific Binding of Tetratricopeptide Repeat Proteins to Heat Shock Protein 70 (Hsp70) and Heat Shock Protein 90 (Hsp90) Is Regulated by Affinity and Phosphorylation. Biochemistry 54, 7120–7131. [PubMed: 26565746]

Blair LJ, Nordhues BA, Hill SE, Scaglione KM, O'Leary JC 3rd, Fontaine SN, Breydo L, Zhang B, Li P, Wang L, et al. (2013). Accelerated neurodegeneration through chaperone-mediated oligomerization of tau. J Clin Invest 123, 4158–4169. [PubMed: 23999428]

Casanal A, Lohkamp B, and Emsley P (2020). Current developments in Coot for macromolecular model building of Electron Cryo-microscopy and Crystallographic Data. Protein Sci 29, 1069–1078. [PubMed: 31730249]

Cheung-Flynn J, Roberts PJ, Riggs DL, and Smith DF (2003). C-terminal sequences outside the tetratricopeptide repeat domain of FKBP51 and FKBP52 cause differential binding to Hsp90. J Biol Chem 278, 17388–17394. [PubMed: 12611898]

Connarn JN, Assimon VA, Reed RA, Tse E, Southworth DR, Zuiderweg ER, Gestwicki JE, and Sun D (2014). The molecular chaperone Hsp70 activates protein phosphatase 5 (PP5) by binding the tetratricopeptide repeat (TPR) domain. J Biol Chem 289, 2908–2917. [PubMed: 24327656]

Croll TI (2018). ISOLDE: a physically realistic environment for model building into low-resolution electron-density maps. Acta Crystallogr D Struct Biol 74, 519–530. [PubMed: 29872003]

Cunningham CN, Southworth DR, Krukenberg KA, and Agard DA (2012). The conserved arginine 380 of Hsp90 is not a catalytic residue, but stabilizes the closed conformation required for ATP hydrolysis. Protein Sci 21, 1162–1171. [PubMed: 22653663]

de la Rosa-Trevin JM, Quintana A, Del Cano L, Zaldivar A, Foche I, Gutierrez J, Gomez-Blanco J, Burguet-Castell J, Cuenca-Alba J, Abrishami V, et al. (2016). Scipion: A software framework toward integration, reproducibility and validation in 3D electron microscopy. J Struct Biol 195, 93–99. [PubMed: 27108186]

Ebong IO, Beilsten-Edmands V, Patel NA, Morgner N, and Robinson CV (2016). The interchange of immunophilins leads to parallel pathways and different intermediates in the assembly of Hsp90 glucocorticoid receptor complexes. Cell Discov 2, 16002. [PubMed: 27462449]

Frenz B, Walls AC, Egelman EH, Veesler D, and DiMaio F (2017). RosettaES: a sampling strategy enabling automated interpretation of difficult cryo-EM maps. Nat Methods 14, 797–800. [PubMed: 28628127]

Genest O, Reidy M, Street TO, Hoskins JR, Camberg JL, Agard DA, Masison DC, and Wickner S (2013). Uncovering a region of heat shock protein 90 important for client binding in E. coli and chaperone function in yeast. Mol Cell 49, 464–473. [PubMed: 23260660]

Grad I, and Picard D (2007). The glucocorticoid responses are shaped by molecular chaperones. Mol Cell Endocrinol 275, 2–12. [PubMed: 17628337]

Hahle A, Merz S, Meyners C, and Hausch F (2019). The Many Faces of FKBP51. Biomolecules 9.

Henderson R, Sali A, Baker ML, Carragher B, Devkota B, Downing KH, Egelman EH, Feng Z, Frank J, Grigorieff N, et al. (2012). Outcome of the first electron microscopy validation task force meeting. Structure 20, 205–214. [PubMed: 22325770]

Huck JD, Que NL, Hong F, Li Z, and Gewirth DT (2017). Structural and Functional Analysis of GRP94 in the Closed State Reveals an Essential Role for the Pre-N Domain and a Potential Client-Binding Site. Cell Rep 20, 2800–2809. [PubMed: 28930677]

Jinwal UK, Koren J 3rd, Borysov SI, Schmid AB, Abisambra JF, Blair LJ, Johnson AG, Jones JR, Shults CL, O'Leary JC 3rd, et al. (2010). The Hsp90 cochaperone, FKBP51, increases Tau stability and polymerizes microtubules. J Neurosci 30, 591–599. [PubMed: 20071522]

Johnson JL, and Toft DO (1994). A novel chaperone complex for steroid receptors involving heat shock proteins, immunophilins, and p23. J Biol Chem 269, 24989–24993. [PubMed: 7929183]

Karagoz GE, Duarte AM, Akoury E, Ippel H, Biernat J, Moran Luengo T, Radli M, Didenko T, Nordhues BA, Veprintsev DB, et al. (2014). Hsp90-Tau complex reveals molecular basis for specificity in chaperone action. Cell 156, 963–974. [PubMed: 24581495]

Kaziales A, Barkovits K, Marcus K, and Richter K (2020). Glucocorticoid receptor complexes form cooperatively with the Hsp90 co-chaperones Pp5 and FKBPs. Sci Rep 10, 10733. [PubMed: 32612187]

Kumar R, Moche M, Winblad B, and Pavlov PF (2017). Combined x-ray crystallography and computational modeling approach to investigate the Hsp90 C-terminal peptide binding to FKBP51. Sci Rep 7, 14288. [PubMed: 29079741]

Lavery LA, Partridge JR, Ramelot TA, Elnatan D, Kennedy MA, and Agard DA (2014). Structural asymmetry in the closed state of mitochondrial Hsp90 (TRAP1) supports a two-step ATP hydrolysis mechanism. Mol Cell 53, 330–343. [PubMed: 24462206]

Lennon CW, Ross W, Martin-Tumasz S, Toulokhonov I, Vrentas CE, Rutherford ST, Lee JH, Butcher SE, and Gourse RL (2012). Direct interactions between the coiled-coil tip of DksA and the trigger loop of RNA polymerase mediate transcriptional regulation. Genes Dev 26, 2634–2646. [PubMed: 23207918]

Liebschner D, Afonine PV, Baker ML, Bunkoczi G, Chen VB, Croll TI, Hintze B, Hung LW, Jain S, McCoy AJ, et al. (2019). Macromolecular structure determination using X-rays, neutrons and electrons: recent developments in Phenix. Acta Crystallogr D Struct Biol 75, 861–877. [PubMed: 31588918]

Meyer P, Prodromou C, Liao C, Hu B, Mark Roe S, Vaughan CK, Vlasic I, Panaretou B, Piper PW, and Pearl LH (2004). Structural basis for recruitment of the ATPase activator Aha1 to the Hsp90 chaperone machinery. Embo J 23, 511–519. [PubMed: 14739935]

Minami Y, Kimura Y, Kawasaki H, Suzuki K, and Yahara I (1994). The carboxy-terminal region of mammalian HSP90 is required for its dimerization and function in vivo. Mol Cell Biol 14, 1459–1464. [PubMed: 8289821]

Nair SC, Rimerman RA, Toran EJ, Chen S, Prapapanich V, Butts RN, and Smith DF (1997). Molecular cloning of human FKBP51 and comparisons of immunophilin interactions with Hsp90 and progesterone receptor. Mol Cell Biol 17, 594–603. [PubMed: 9001212]

Ni L, Yang CS, Gioeli D, Frierson H, Toft DO, and Paschal BM (2010). FKBP51 promotes assembly of the Hsp90 chaperone complex and regulates androgen receptor signaling in prostate cancer cells. Mol Cell Biol 30, 1243–1253. [PubMed: 20048054]

Nikolovska-Coleska Z, Wang R, Fang X, Pan H, Tomita Y, Li P, Roller PP, Krajewski K, Saito NG, Stuckey JA, et al. (2004). Development and optimization of a binding assay for the XIAP BIR3 domain using fluorescence polarization. Anal Biochem 332, 261–273. [PubMed: 15325294]

Noddings CM, Wang RY-R, and Agard DA (2020). GR chaperone cycle mechanism revealed by cryo-EM: reactivation of GR by the GR:Hsp90:p23 client-maturation complex. bioRxiv, 2020.2009.2012.294975.

Oroz J, Chang BJ, Wysoczanski P, Lee CT, Perez-Lara A, Chakraborty P, Hofele RV, Baker JD, Blair LJ, Biernat J, et al. (2018). Structure and pro-toxic mechanism of the human Hsp90/PPIase/Tau complex. Nat Commun 9, 4532. [PubMed: 30382094]

Pettersen EF, Goddard TD, Huang CC, Couch GS, Greenblatt DM, Meng EC, and Ferrin TE (2004). UCSF Chimera--a visualization system for exploratory research and analysis. J Comput Chem 25, 1605–1612. [PubMed: 15264254]

Pettersen EF, Goddard TD, Huang CC, Meng EC, Couch GS, Croll TI, Morris JH, and Ferrin TE (2021). UCSF ChimeraX: Structure visualization for researchers, educators, and developers. Protein Sci 30, 70–82. [PubMed: 32881101]

Pratt WB, and Toft DO (1997). Steroid receptor interactions with heat shock protein and immunophilin chaperones. Endocr Rev 18, 306–360. [PubMed: 9183567]

Prodromou C, Panaretou B, Chohan S, Siligardi G, O'Brien R, Ladbury JE, Roe SM, Piper PW, and Pearl LH (2000). The ATPase cycle of Hsp90 drives a molecular 'clamp' via transient dimerization of the N-terminal domains. Embo J 19, 4383–4392. [PubMed: 10944121]

Punjani A, Rubinstein JL, Fleet DJ, and Brubaker MA (2017). cryoSPARC: algorithms for rapid unsupervised cryo-EM structure determination. Nat Methods 14, 290–296. [PubMed: 28165473]

Ravalin M, Theofilas P, Basu K, Opoku-Nsiah KA, Assimon VA, Medina-Cleghorn D, Chen YF, Bohn MF, Arkin M, Grinberg LT, et al. (2019). Specificity for latent C termini links the E3 ubiquitin ligase CHIP to caspases. Nat Chem Biol 15, 786–794. [PubMed: 31320752]

Richter K, Soroka J, Skalniak L, Leskovar A, Hessling M, Reinstein J, and Buchner J (2008). Conserved conformational changes in the ATPase cycle of human Hsp90. J Biol Chem 283, 17757–17765. [PubMed: 18400751]

Richter K, Walter S, and Buchner J (2004). The Co-chaperone Sba1 connects the ATPase reaction of Hsp90 to the progression of the chaperone cycle. J Mol Biol 342, 1403–1413. [PubMed: 15364569]

Riggs DL, Cox MB, Tardif HL, Hessling M, Buchner J, and Smith DF (2007). Noncatalytic role of the FKBP52 peptidyl-prolyl isomerase domain in the regulation of steroid hormone signaling. Mol Cell Biol 27, 8658–8669. [PubMed: 17938211]

Riggs DL, Roberts PJ, Chirillo SC, Cheung-Flynn J, Prapapanich V, Ratajczak T, Gaber R, Picard D, and Smith DF (2003). The Hsp90-binding peptidylprolyl isomerase FKBP52 potentiates glucocorticoid signaling in vivo. EMBO J 22, 1158–1167. [PubMed: 12606580]

Ruiz-Estevez M, Staats J, Paatela E, Munson D, Katoku-Kikyo N, Yuan C, Asakura Y, Hostager R, Kobayashi H, Asakura A, et al. (2018). Promotion of Myoblast Differentiation by Fkbp5 via Cdk4 Isomerization. Cell Rep 25, 2537–2551 e2538. [PubMed: 30485818]

Ryu Y, and Schultz PG (2006). Efficient incorporation of unnatural amino acids into proteins in Escherichia coli. Nat Methods 3, 263–265. [PubMed: 16554830]

Scheres SH (2012). RELION: implementation of a Bayesian approach to cryo-EM structure determination. J Struct Biol 180, 519–530. [PubMed: 23000701]

Scheufler C, Brinker A, Bourenkov G, Pegoraro S, Moroder L, Bartunik H, Hartl FU, and Moarefi I (2000). Structure of TPR domain-peptide complexes: critical elements in the assembly of the Hsp70-Hsp90 multichaperone machine. Cell 101, 199–210. [PubMed: 10786835]

Schopf FH, Biebl MM, and Buchner J (2017). The HSP90 chaperone machinery. Nat Rev Mol Cell Biol 18, 345–360. [PubMed: 28429788]

Shiau AK, Harris SF, Southworth DR, and Agard DA (2006). Structural Analysis of E. coli hsp90 reveals dramatic nucleotide-dependent conformational rearrangements. Cell 127, 329–340. [PubMed: 17055434]

Siligardi G, Hu B, Panaretou B, Piper PW, Pearl LH, and Prodromou C (2004). Co-chaperone regulation of conformational switching in the Hsp90 ATPase cycle. J Biol Chem 279, 51989–51998. [PubMed: 15466438]

Sinars CR, Cheung-Flynn J, Rimerman RA, Scammell JG, Smith DF, and Clardy J (2003). Structure of the large FK506-binding protein FKBP51, an Hsp90-binding protein and a component of steroid receptor complexes. Proc Natl Acad Sci U S A 100, 868–873. [PubMed: 12538866]

Smith MC, Scaglione KM, Assimon VA, Patury S, Thompson AD, Dickey CA, Southworth DR, Paulson HL, Gestwicki JE, and Zuiderweg ER (2013). The E3 ubiquitin ligase CHIP and the molecular chaperone Hsc70 form a dynamic, tethered complex. Biochemistry 52, 5354–5364. [PubMed: 23865999]

Song Y, DiMaio F, Wang RY, Kim D, Miles C, Brunette T, Thompson J, and Baker D (2013). High-resolution comparative modeling with RosettaCM. Structure 21, 1735–1742. [PubMed: 24035711]

Southworth DR, and Agard DA (2008). Species-dependent ensembles of conserved conformational states define the Hsp90 chaperone ATPase cycle. Molecular cell 32, 631–640. [PubMed: 19061638]

Southworth DR, and Agard DA (2011). Client-loading conformation of the Hsp90 molecular chaperone revealed in the cryo-EM structure of the human Hsp90:Hop complex. Molecular cell 42, 771–781. [PubMed: 21700222]

Storer CL, Dickey CA, Galigniana MD, Rein T, and Cox MB (2011). FKBP51 and FKBP52 in signaling and disease. Trends Endocrinol Metab 22, 481–490. [PubMed: 21889356]

Verba KA, Wang RY, Arakawa A, Liu Y, Shirouzu M, Yokoyama S, and Agard DA (2016). Atomic structure of Hsp90-Cdc37-Cdk4 reveals that Hsp90 traps and stabilizes an unfolded kinase. Science 352, 1542–1547. [PubMed: 27339980]

Wang RY-R, Noddings CM, Kirschke E, Myasnikov AG, Johnson JL, and Agard DA (2020). GR chaperone cycle mechanism revealed by cryo-EM: inactivation of GR by GR:Hsp90:Hsp70:Hop client-loading complex. bioRxiv, 2020.2011.2005.370247.

Waterhouse A, Bertoni M, Bienert S, Studer G, Tauriello G, Gumienny R, Heer FT, de Beer TAP, Rempfer C, Bordoli L, et al. (2018). SWISS-MODEL: homology modelling of protein structures and complexes. Nucleic Acids Res 46, W296–W303. [PubMed: 29788355]

Weaver AJ, Sullivan WP, Felts SJ, Owen BA, and Toft DO (2000). Crystal structure and activity of human p23, a heat shock protein 90 co-chaperone. J Biol Chem 275, 23045–23052. [PubMed: 10811660]

Wilkinson ME, Kumar A, and Casanal A (2019). Methods for merging data sets in electron cryo-microscopy. Acta Crystallogr D Struct Biol 75, 782–791. [PubMed: 31478901]

Wochnik GM, Ruegg J, Abel GA, Schmidt U, Holsboer F, and Rein T (2005). FK506-binding proteins 51 and 52 differentially regulate dynein interaction and nuclear translocation of the glucocorticoid receptor in mammalian cells. J Biol Chem 280, 4609–4616. [PubMed: 15591061]

Wu B, Li P, Liu Y, Lou Z, Ding Y, Shu C, Ye S, Bartlam M, Shen B, and Rao Z (2004). 3D structure of human FK506-binding protein 52: implications for the assembly of the glucocorticoid receptor/Hsp90/immunophilin heterocomplex. Proc Natl Acad Sci U S A 101, 8348–8353. [PubMed: 15159550]

Zgajnar NR, De Leo SA, Lotufo CM, Erlejman AG, Piwien-Pilipuk G, and Galigniana MD (2019). Biological Actions of the Hsp90-binding Immunophilins FKBP51 and FKBP52. Biomolecules 9.

Zhang H, Amick J, Chakravarti R, Santarriaga S, Schlanger S, McGlone C, Dare M, Nix JC, Scaglione KM, Stuehr DJ, et al. (2015). A bipartite interaction between Hsp70 and CHIP regulates ubiquitination of chaperoned client proteins. Structure 23, 472–482. [PubMed: 25684577]

Zheng SQ, Palovcak E, Armache JP, Verba KA, Cheng Y, and Agard DA (2017). MotionCor2: anisotropic correction of beam-induced motion for improved cryo-electron microscopy. Nat Methods 14, 331–332. [PubMed: 28250466]

Highlights

- Structure of Hsp90:FKBP51:p23 reveals chaperone state for client maturation.
- FKBP51 specifically binds the closed, ATP state of Hsp90 via TPR domain contacts.
- The C-terminal helix extension of FKBP51 serves as an Hsp90 recognition element.
- Positioning FKBP51 PPIase domain adjacent client binding may assist in refolding.

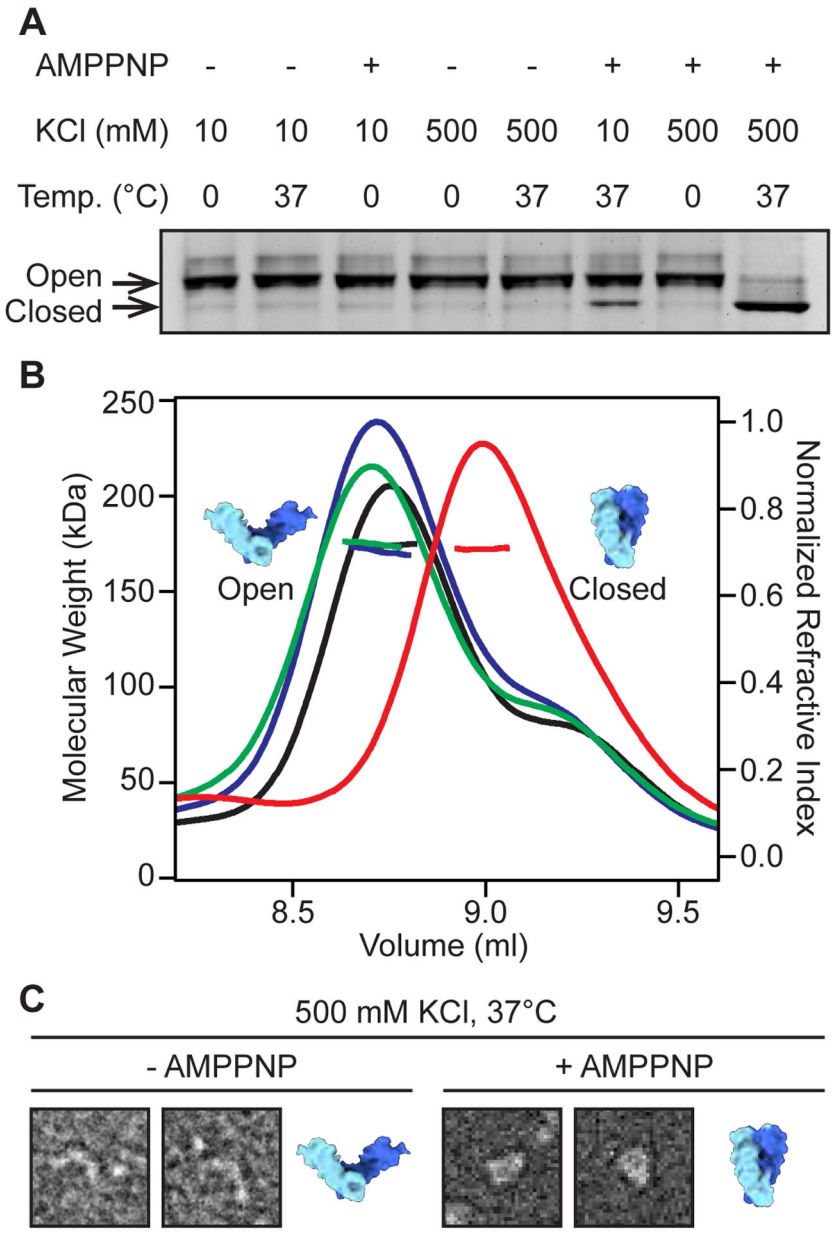

Figure 1. Analysis of Hsp90 in the open and closed states.

(A) Native-gel of Hsp90 following incubation under indicated temperature, KCl and nucleotide (2 mM AMPPNP) conditions. Two independent experiments were performed. (B) SEC-MALS (in 150 mM KCl) of Hsp90 following incubation at 37°C with no nucleotide in 500 mM KCl (black), at 0°C with 2 mM AMPPNP in 500 mM KCl (green), at 37°C with 2 mM AMPPNP in 8 mM KCl (blue), and at 37°C with 2 mM AMPPNP in 500 mM KCl (red). The mw_{avg} is indicated by horizontal lines (kDa, left Y-axis), and is shown with the elution trace of the protein concentration (refractive index, right Y-axis) versus elution volume (ml). (C) Representative negative-stain single particle images of Hsp90 following incubation with 500 mM KCl at 37°C in the absence (left) and presence (right) of 2 mM

AMPPNP and compared to structures of the Hsp90 dimer in the open (PDB: 2IOQ) and closed (PDB: 2CG9) states.

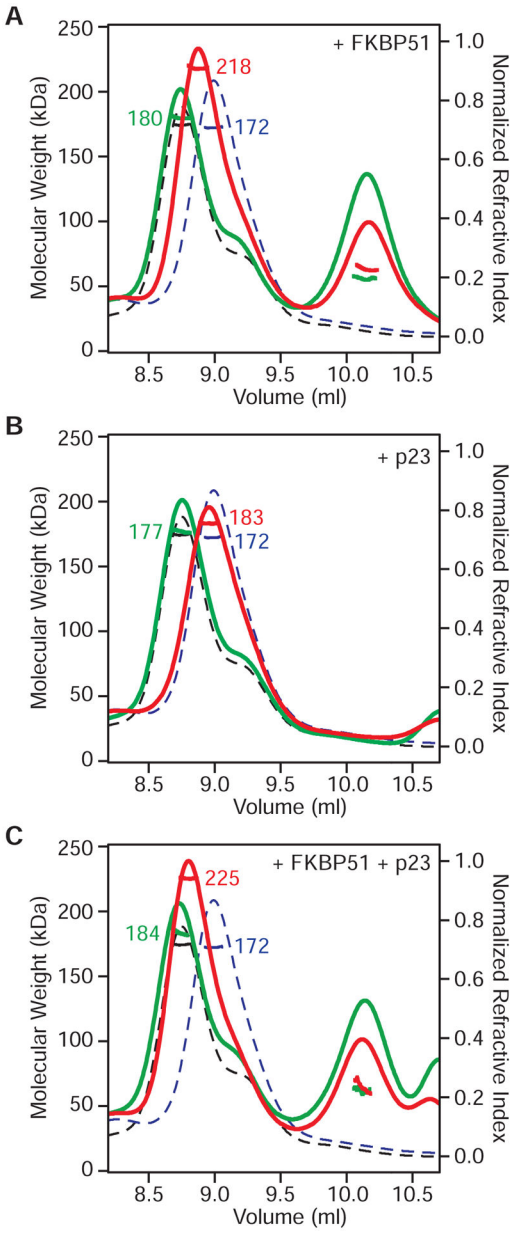

Figure 2. SEC-MALS of FKBP51 and p23 binding to Hsp90 in the open and closed states.

(A) FKBP51, (B) p23, or (C) FKBP51 with p23 were incubated with Hsp90 at 37°C in 500 mM KCl under open-state (green) or closed-state (with 2 mM AMPPNP) (red) conditions and compared to Hsp90 alone in the open (black, dashed) and closed (blue, dashed) states. Axes are shown as in Figure 1 and the mw_{avg} (kDa) determined by MALS, is shown for the corresponding Hsp90 complex.

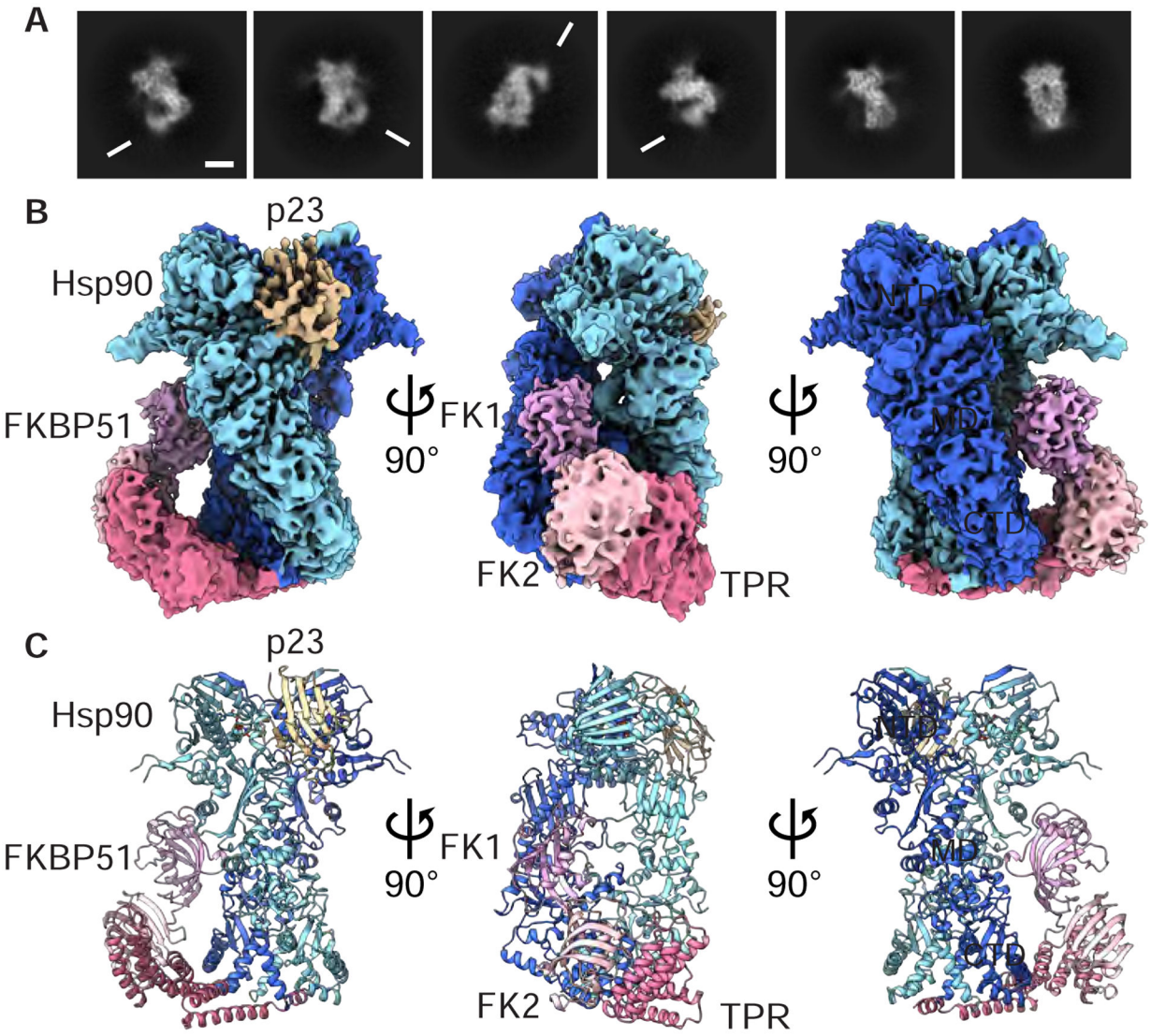

Figure 3. Cryo-EM structure of Hsp90:FKBP51:p23 closed-state complex.

(A) Example 2D class averages of Hsp90:FKBP51:p23 (scale bar = 50 Å). The Hsp90 domains are labeled and FKBP51 density is shown (arrow) adjacent the CTD. (B) The final cryo-EM map of Hsp90:FKBP51:p23. Densities are colored based on the molecular model and correspond to the Hsp90 monomers (light and dark blue), the FKBP51 domains: FK1 (plum), FK2 (light pink) and the TPR (dark pink), and p23 (tan). (C) The final molecular model of Hsp90:FKBP51:p23 colored as in (B).

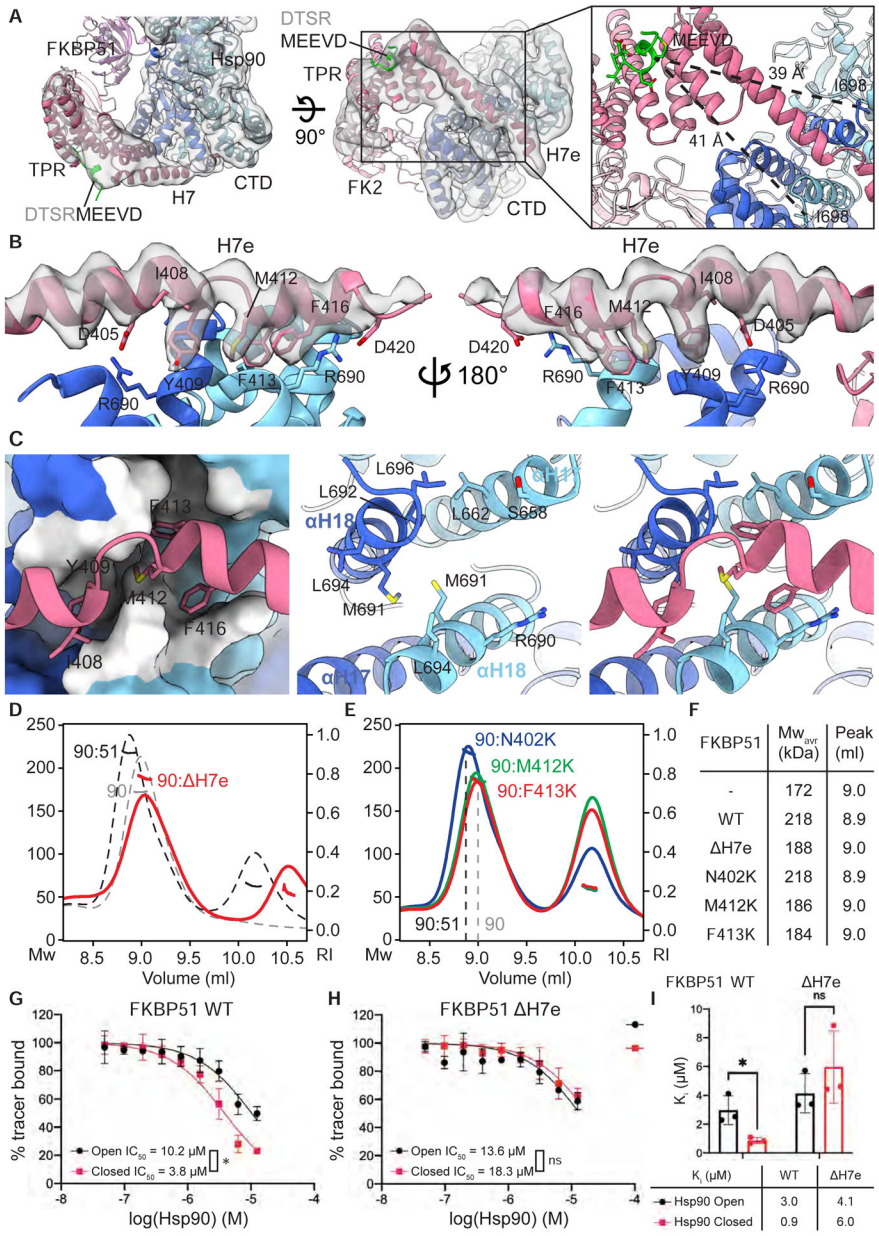

Figure 4. Interactions by the FKBP51 TPR helix 7 extension (H7e) and the Hsp90 CTD define the closed state interaction.

(A) Low-pass filtered cryo-EM density map and model of Hsp90:FKBP51:p23 showing the CTD-TPR interaction, colored as in Figure 3 with the Hsp90 MEEVD peptide (green) modeled based on PDB 5NJX (Kumar et al., 2017). Expanded view (right panel) with approximate distances between M728 from the MEEVD and the Hsp90 C-terminal residue, I698, identified in the structure (dashed lines). (B) View of H7e (map+model) interacting across the Hsp90 CTD dimer interface. Proposed H7e hydrophobic interacting residues are labeled along with D405 and D420 residues which contact Hsp90 R690. (C) Surface representation of the Hsp90 CTD dimer groove is shown with hydrophobic residues in white and ribbon view of H7e (left panel); view of Hsp90 CTD dimer interface helices αH17 and αH18 and proposed interacting residues shown without (middle) and with H7e (right).

(D,E) SEC-MALS analysis and (F) summary table of Hsp90:FKBP51 complex formation under closed state conditions with FKBP51 variants: (D) ΔH7e (Δ401–457) (red), and (E) M412K (green), F413K (red), and N402K (blue) in comparison to wildtype closed state complexes of Hsp90 (grey) and Hsp90:FKBP51 (black). The mw_{avg} (left Y axis) and protein concentration (right Y axis) are shown versus elution volume (ml). Competitive binding inhibition of fluorescence polarization of FAM-DDTSRMEEVD bound to (G) FKBP51 wt or (H) ΔH7e by Hsp90 pre-incubated in the (red) closed or (black) open state conditions. Data are shown as the % tracer bound vs. the Hsp90 concentration. IC_{50} values of 3.8 and 10.2 μM and (I) K_i values of 0.9 ± 0.2 and 3.0 ± 1.0 μM were determined for FKBP51 wt with closed and open-state Hsp90 additions, respectively. IC_{50} values of 18.3 and 13.6 μM and (I) K_i values of 6.0 ± 2.5 and 4.1 ± 1.4 μM were determined for FKBP51 ΔH7e with closed and open-state Hsp90 additions, respectively. Three independent experiments were performed. Error bars represent standard deviation. *$p < 0.5$, ns = no significance.

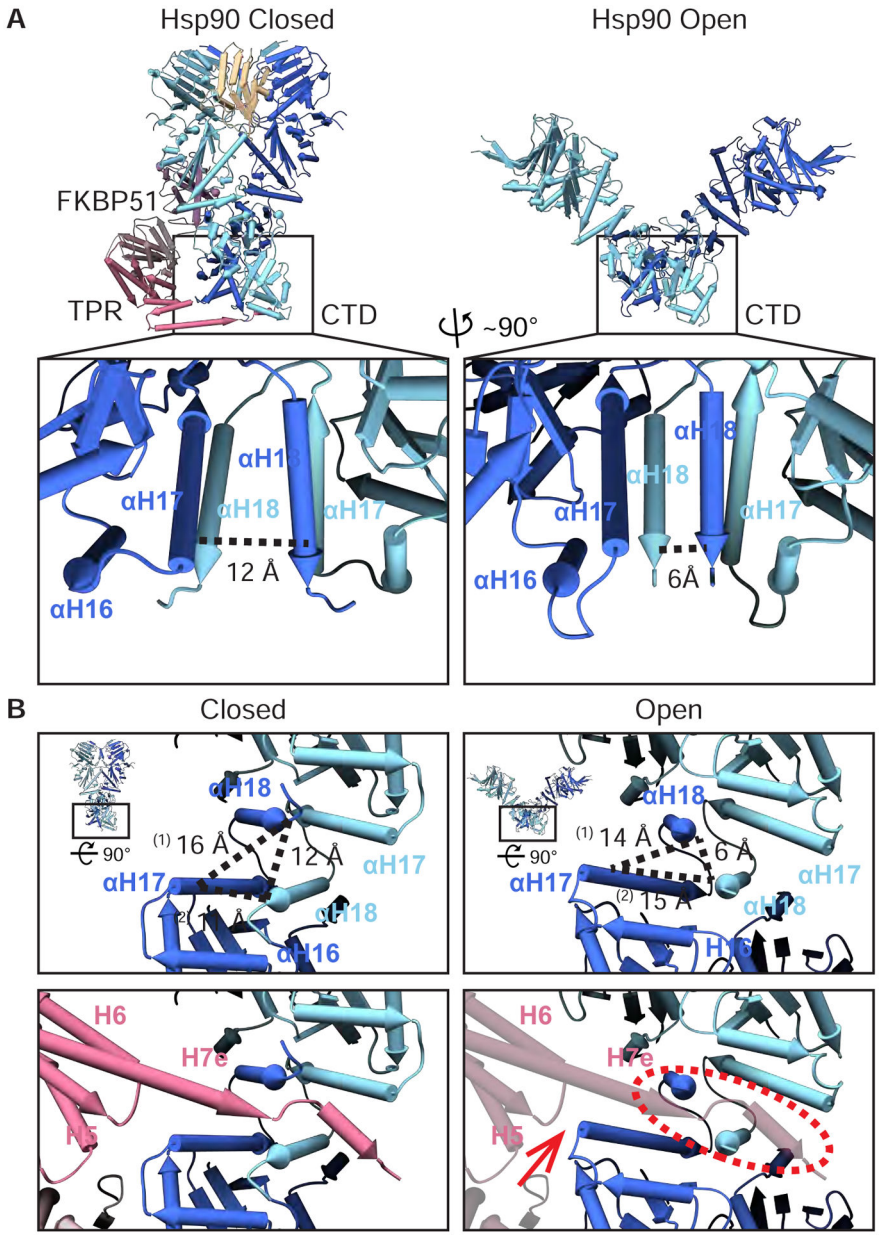

Figure 5. Comparison of Hsp90 CTD conformations showing accommodation of FKBP51 H7e is specific to the closed state.

(A) Closed- (Hsp90:FKBP51:p23) and open-state (*E. coli* HtpG, PDB: 2IOQ) (Ali et al., 2006) Hsp90 structures with an expanded view of the CTD dimer showing distances between αH17 and αH18 (dashed line), indicating a wider dimer cleft in the closed state. (B) Rotated view of the CTD dimer in the closed (left) and open (right) states showing additional distances between αH17 and αH18 (dashed lines). Measurements are between S658 (αH17) and I692 (αH18) in the same subunit (1), across subunits (2). FKBP51 TPR (pink) is shown with H7e bound across the Hsp90 CTD dimer in the closed state (lower, left panel), as modeled in the Hsp90:FKBP51:p23 structure, but is incompatible and clashes with the CTD in the open state (lower right panel, dashed circle). Additional clashing at the H5 loop is indicated (arrow).

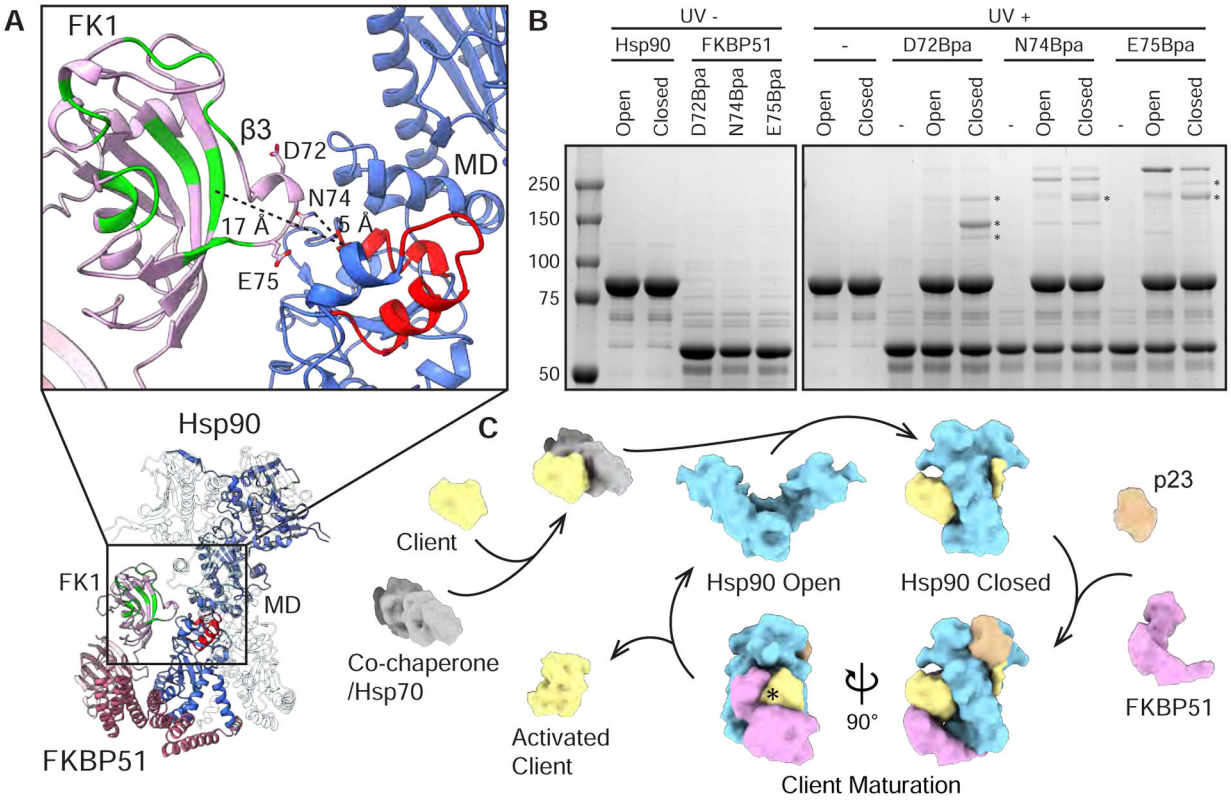

Figure 6. Positioning of FK1 PPIase domain adjacent Hsp90 client binding sites and model for FKBP51 function during client maturation.

(A) The Hsp90:FKBP51:p23 structure with distances showing the FK1 PPIase site and FK506 binding pocket (green) and connecting β3 bulge are positioned adjacent MD client binding sites (red) in Hsp90 (blue). Sites of Bpa incorporation in the β3 bulge region are shown. (B) SDS-PAGE analysis of Hsp90-FKBP51 photocrosslinking using FKBP51 variants with Bpa at D72, N74, or E75 following incubation under closed and open state conditions. Unique crosslinking bands present under closed-state conditions are indicated (asterisks). Two independent experiments were conducted. (C) Model for Hsp90-catalyzed client maturation and activation based on the Hsp90:FKBP51:p23 structure in which FKBP51 binds Hsp90 with p23 following ATP binding and NTD dimerization to form the client maturation complex. In this arrangement, FKBP51 is positioned for PPIase activity directed at specific client sites presented through Hsp90 binding and remodeling. Colors: Hsp90=light blue, FKBP51=pink, p23=tan, Client=yellow, Co-chaperone/Hsp70=Grey.

Table 1.

Cryo-EM data collection, processing and validation

	Hsp90:FKBP51:p23 (EMD-23213, PDB 7L7I)	Hsp90:p23 (EMD-23214,PDB 7L7J)
Data collection and processing		
Microscope and camera	Titan Krios and K2 or K3	
Magnification	61425 (K2), 58600 (K3)	
Voltage (kV)	300	
Data acquisition software	Serial EM	
Exposure navigation	Image shift	
Electron exposure (e^{-}/Å^2)	70 (K2), 66 (K3)	
Defocus range (μm)	−2.0 to −1.0	
Pixel size (Å)	0.814	
Symmetry imposed	C1	
Initial particle images (no.)	576169	
Final particle images (no.)	121882	239079
Map resolution (Å)	3.3	3.1
FSC threshold	0.143	0.143
Map resolution range (Å)	2–10	2–10
Refinement		
Model resolution (Å)	3.7	3.3
FSC threshold	0.5	0.5
Map sharpening B factor (Å^2)	−100.4	−109.8
Model composition		
Nonhydrogen atoms	14429	11199
Protein residues	1775	1366
Ligands	2	2
B factors (Å^2)		
Protein	40.53	38.40
Ligand	38.44	38.44
R.m.s. deviations		
Bond lengths (Å)	0.013	0.013
Bond angles (°)	1.878	1.889
Validation		
MolProbity score	1.14	1.19
Clashscore	1.39	1.47
Poor rotamers (%)	0.76	0.73
Ramachandran plot		
Favored (%)	96.09	95.58
Allowed (%)	3.74	4.28

	Hsp90:FKBP51:p23 (EMD-23213, PDB 7L7I)	Hsp90:p23 (EMD-23214,PDB 7L7J)
Disallowed (%)	0.17	0.15

KEY RESOURCES TABLE

REAGENT or RESOURCE	SOURCE	IDENTIFIER
Bacterial and virus strains		
BL21-AI™ One Shot™ Chemically Competent *E. coli*	Invitrogen	Cat# C607003
BL21 Star™ (DE3)pLysS One Shot™ Chemically Competent *E. coli*	Invitrogen	Cat# C602003
Chemicals, peptides, and recombinant proteins		
Adenosine 5'-(β,γ-imido)triphosphate lithium salt hydrate	Sigma-Aldrich	Cat# A2647
Glutaraldehyde	Electron Microscopy Sciences	Cat# 16019
4-Benzoyl-L-phenylalanine	Alfa Aesar	Cat# H52083-03
FAM-DDTSRMEEVD	(Assimon et al., 2015)	N/A
Deposited data		
Atomic coordinates of Hsp90:FKBP51:p23 closed-state complex	This paper	PDB: 7L7I
Cryo-EM density of Hsp90:FKBP51:p23 closed-state complex	This paper	EMD: 23213
Atomic coordinates of Hsp90:p23 closed-state complex	This paper	PDB: 7L7J
Cryo-EM density of Hsp90:p23 closed-state complex	This paper	EMD: 23214
Atomic coordinates of full-length HTPG, the *Escherichia coli* HSP90	(Shiau et al., 2006)	PDB: 2IOQ
Atomic coordinates of an Hsp90-Sba1 closed chaperone complex	(Ali et al., 2006)	PDB: 2CG9
Atomic coordinates of human FKBP51 protein in complex with C-terminal peptide of human HSP 90-alpha	(Kumar et al., 2017)	PDB: 5NJX
Atomic coordinates of Hsp90-Cdc37-Cdk4 complex	(Verba et al., 2016)	PDB: 5FWK
Atomic coordinates of the human co-chaperone p23	(Weaver et al., 2000)	PDB: 1EJF
Recombinant DNA		
pET151-Hsp90α	(Southworth and Agard, 2008)	N/A
pET151-FKBP51	This paper	N/A
pET151-FKBP51 del401–457	This paper	N/A
pET151-FKBP51 N402K	This paper	N/A
pET151-FKBP51 M412K	This paper	N/A
pET151-FKBP51 F413K	This paper	N/A
pET151-FKBP51 E23TAG	This paper	N/A
pET151-FKBP51 S27TAG	This paper	N/A
pET151-FKBP51 K29TAG	This paper	N/A
pET151-FKBP51 D72TAG	This paper	N/A
pET151-FKBP51 N74TAG	This paper	N/A
pET151-FKBP51 E75TAG	This paper	N/A
pET151-p23	This paper	N/A
pSUPT/BpF	(Lennon et al., 2012)	N/A

REAGENT or RESOURCE	SOURCE	IDENTIFIER
Software and algorithms		
UCSF MotionCor2	(Zheng et al., 2017)	https://emcore.ucsf.edu/ucsf-software
Scipion	(de la Rosa-Trevin et al., 2016)	http://scipion.i2pc.es/
cryoSPARC2 v3.1.0	(Punjani et al., 2017)	https://cryosparc.com/
Relion	(Scheres, 2012)	https://www3.mrc-lmb.cam.ac.uk/relion/index.php/Main_Page
SWISS-MODEL	(Waterhouse et al., 2018)	https://swissmodel.expasy.org/
RosettaCM	(Song et al., 2013)	https://new.rosettacommons.org/docs/latest/application_documentation/structure_prediction/RosettaCM
RosettaES	(Frenz et al., 2017)	https://dimaiolab.ipd.uw.edu/software/
ISOLDE	(Croll, 2018)	https://isolde.cimr.cam.ac.uk/
Coot	(Casanal et al., 2020)	https://www2.mrc-lmb.cam.ac.uk/personal/pemsley/coot/
Phenix 1.19.1	(Afonine et al., 2018)	http://www.phenix-online.org/
UCSF Chimera	(Pettersen et al., 2004)	https://www.cgl.ucsf.edu/chimera/
UCSF ChimeraX	(Pettersen et al., 2021)	https://www.rbvi.ucsf.edu/chimerax/